

THE CONNECTION BETWEEN GALAXIES AND INTERGALACTIC ABSORPTION LINES AT REDSHIFT $2 \lesssim Z \lesssim 3^1$

KURT L. ADELBERGER²

Carnegie Observatories, 813 Santa Barbara St., Pasadena, CA, 91101

ALICE E. SHAPLEY³

University of California, Department of Astronomy, 601 Campbell Hall, Berkeley, CA 94720

CHARLES C. STEIDEL

Palomar Observatory, Caltech 105–24, Pasadena, CA 91125

MAX PETTINI

Institute of Astronomy, Madingley Road, Cambridge CB3 0HA, UK

DAWN K. ERB & NAVEEN A. REDDY

Palomar Observatory, Caltech 105–24, Pasadena, CA 91125

Draft version November 18, 2018

ABSTRACT

Absorption-line spectroscopy of 23 background QSOs and numerous background galaxies has let us measure the spatial distribution of metals and neutral hydrogen around 1044 UV-selected galaxies at redshifts $1.8 \lesssim z \lesssim 3.3$. The typical galaxy is surrounded to radii $r \sim 40$ proper kpc by gas that has a large velocity spread ($\Delta v > 260$ km s⁻¹) and produces very strong absorption lines ($N_{\text{CIV}} \gg 10^{14}$ cm⁻²) in the spectra of background objects. These absorption lines are almost as strong as those produced by a typical galaxy’s own interstellar gas. Absorption with an average column density of $N_{\text{CIV}} \simeq 10^{14}$ cm⁻² extends to ~ 80 kpc, a radius large enough to imply that most strong intergalactic CIV absorption is associated with star-forming galaxies like those in our sample. Our measurement of the galaxy/CIV spatial correlation function shows that even the weakest detectable CIV systems are found in the same regions as galaxies; we find that the cross-correlation length increases with CIV column density and is similar to the galaxy auto-correlation length ($r_0 \sim 4h^{-1}$ Mpc) for $N_{\text{CIV}} \gtrsim 10^{12.5}$ cm⁻². Distortions in the redshift-space galaxy-CIV correlation function on small scales may imply that some of the CIV systems have large peculiar velocities. Four of the five detected OVI absorption systems in our sample lie within 400 proper kpc of a known galaxy. Strong Lyman- α absorption is produced by the intergalactic gas within $1h^{-1}$ comoving Mpc of most galaxies, but for a significant minority ($\sim 1/3$) the absorption is weak or absent. This is not observed in SPH simulations that omit the effects of “feedback” from galaxy formation. We were unable to identify any statistically significant differences in age, dust reddening, environment, or kinematics between galaxies with weak nearby HI absorption and the rest, although galaxies with weak absorption may have higher star-formation rates. Galaxies near intergalactic CIV systems appear to reside in relatively dense environments and to have distinctive spectral energy distributions that are characterized by blue colors and young ages.

Subject headings: galaxies: formation — galaxies: high-redshift — intergalactic medium — quasars: absorption lines

1. INTRODUCTION

A tremendous amount of gravitational energy is released when a massive galaxy forms, roughly 10^{62} erg from its billion supernova explosions and another 10^{62} erg during the assembly of its central 10^8 - M_{\odot} black hole. Although 99% of the supernova energy is carried away by neutrinos, and a similar fraction of the black hole radia-

tion escapes the galaxy, the remaining energy is enough to unbind most of the galaxy’s gas. The fate of the galaxy depends on what happens to the energy. If it is absorbed by sufficiently dense gas, it will be converted into radiation by two-body processes and will stream harmlessly away; but otherwise it will set in motion an enormous blast-wave analogous to those produced by nuclear explosions on earth. These blast-waves, tearing through galaxies, stripping away material, plowing outwards, and coming finally to rest in distant intergalactic space, are believed to have significantly altered the evolution of the baryonic universe.

Indirect evidence for their existence comes in two forms. First, if the gas near galaxies had not been heated

¹ Based, in part, on data obtained at the W.M. Keck Observatory, which is operated as a scientific partnership between the California Institute of Technology, the University of California, and NASA, and was made possible by the generous financial support of the W.M. Keck Foundation.

² Carnegie Fellow

³ Miller Fellow

by some source, disk galaxies would be smaller than they are (Weil, Eke, & Efstathiou 1998) and the correlation between galaxy clusters’ X-ray temperature and luminosity would have the wrong shape (Kaiser 1991; Ponman, Cannon, & Navarro 1999). Second, something quenches most galaxies’ star formation at some point in their history, and blast-waves seem the best candidate. Without them small galaxies would be too numerous (e.g., Cole et al. 1994), big galaxies would be too blue (Springel, Di Matteo, & Hernquist 2005) and too large a fraction of baryons would have been turned into stars (e.g., White & Rees 1978, Springel & Hernquist 2002).

Direct evidence remains elusive, however. Although local star-forming galaxies are surrounded by outflowing gas (e.g., Heckman et al. 1990; Martin 2005), typically their observable outflows extend to only a few kpc, far smaller than their virial radii. It is unclear how far these flows will advance before they stall or how severely they will affect the evolution of the galaxies and their surroundings. The presence of metals in the intergalactic medium might be taken as proof that the blast-waves spill out of some galaxies’ halos, but even that is controversial. Intergalactic metals could also have been produced by the first generation of Population III stars or stripped from galaxies by other processes (e.g., Gnedin 1998).

Five years ago, our group began to search for direct evidence for large-scale outflows around galaxies at high redshift. High-redshift galaxies were attractive targets because they have larger star-formation rates and (possibly) shallower potentials than their nearby counterparts. In addition, the higher density of the universe in the past is a significant advantage, because it strengthens many of the absorption lines that can be used to detect intergalactic gas. We identified three observations that would qualify, in our view, as direct evidence for large-scale outflows: gas at large galactocentric radii moving outwards at greater than the escape velocity; a strong association of intergalactic metals and galaxies; and disturbances, near galaxies, to the lattice-work of intergalactic HI that pervades the high-redshift universe.

We searched for this evidence by systematically mapping the relative spatial distributions of star-forming galaxies and intergalactic gas. Early results were presented in Adelberger et al. (2003). This paper is an update. After describing the current data in § 2, we review the status of our search. Section 3 shows that the outflowing material responsible for the blue-shifted “interstellar” absorption lines in the galaxies’ spectra often lies at a radius of $\sim 20\text{--}40h^{-1}$ proper kpc. Weaker absorption lines extend out to radii approaching $200h^{-1}$ kpc. Section 4 describes the galaxy-CIV cross-correlation function and reinforces the idea that detectable intergalactic metals tend to lie near actively star-forming galaxies. Section 5 shows that most galaxies are surrounded by significant amounts of intergalactic HI but that galaxies with little nearby HI are significantly more common than would be expected in the absence of winds. Section 6 discusses the characteristics of galaxies that appear to be associated with unusually weak Ly- α or unusually strong CIV absorption. As we discuss in § 7, these observations may be suggestive of galactic winds, but they do not rule out other alternatives. Our conclusions are summarized in § 8. Throughout the paper we

TABLE 1. OBSERVED FIELDS

Field	$\Delta\Omega^a$	N_{LRIS}^b	N_{NIRSPEC}^c
Q0000	3.4×4.5	18	1
Q0201	6.8×7.4	25	3
Q0256	7.3×6.6	47	1
Q0302	6.5×6.9	44	1
Q0933	8.1×8.0	64	0
Q1305	11.8×11.0	80	1
Q1422	7.2×14.2	113	1
Q1623	16.1×11.6	213	31
Q1700	11.5×11.0	89	16
Q2233	8.2×8.6	46	1
Q2343	22.5×8.5	194	19
Q2346	10.9×11.0	50	7
SSA22a	7.8×8.4	61	8

^aArea imaged in U_nGR and observed spectroscopically, arcmin²

^bNumber of galaxies with LRIS redshift $z > 1$

^cNumber of galaxies with NIRSPEC redshift $z > 1$

assume a cosmology with $\Omega_M = 0.3$, $\Omega_\Lambda = 0.7$, $h = 0.7$.

2. DATA

The galaxies in our analysis were taken from the redshift surveys of Steidel et al. (2003; 2004). These surveys targeted galaxies with magnitude $\mathcal{R} \lesssim 25.5$ whose U_nGR colors suggested that they had redshift $2 \lesssim z \lesssim 3$ (Adelberger et al. 2004; Steidel et al. 2003). We restricted our analysis to galaxies in the 13 survey fields that contained one or more background QSOs. Although these fields include those previously analyzed by Adelberger et al. (2003), much of the present analysis relies on near-IR nebular redshifts (see below) that are only available in other fields. As a result, the overlap is small between the samples analyzed here and in Adelberger et al. (2003).

Our 13 fields are scattered around the sky and have typical area $\Delta\Omega \sim 100$ arcmin² (Table 1). Redshifts for a total of 1044 objects in these fields were measured from low-resolution ($\sim 10\text{\AA}$) multislit spectra taken between 1995 and 2004 with LRIS (Oke et al. 1995; Steidel et al. 2004) on the Keck I and II 10m telescopes. The typical spectroscopic exposure time was 1.5 hours per multislit mask, although a subset of the objects was observed for more than ten times longer (Shapley et al. 2005, in preparation). The redshifts obtained from these spectra are imprecise, because they rely on features (Ly- α emission and various far-UV interstellar absorption lines) that are redshifted or blueshifted relative to the galaxy’s stars. Erb et al. (2005, in preparation) used NIRSPEC (McLean et al. 2000) on the Keck II telescope to obtain more-precise redshifts from the nebular emission lines ([OII] $\lambda 3727$, H α , H β , [OIII] $\lambda\lambda 4959, 5007$) of 90 galaxies in this sample, many near the sightlines to background QSOs, and we adopt their redshifts wherever possible. If nebular redshifts were unavailable, we estimated the stellar redshifts with the relationships defined in the following paragraph. Precise redshifts were required for much of the analysis, however, and in these cases we ignored galaxies that had not been observed with NIRSPEC.

We measured the relationship between redshifts from Lyman- α emission ($z_{\text{Ly}\alpha}$), interstellar absorption (z_{ISM}), and near-IR nebular emission (z_{neb}) for the full 138-

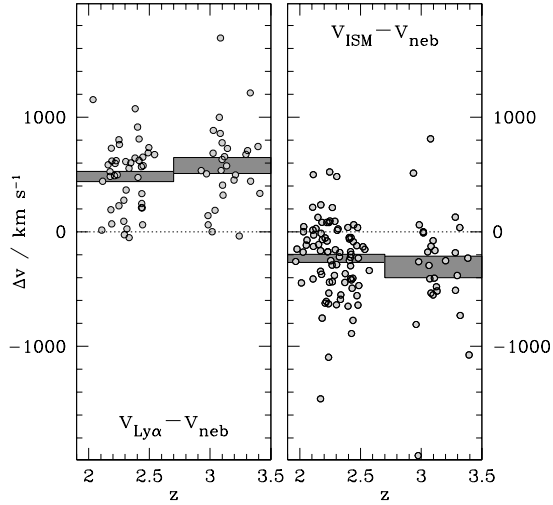


FIG. 1.— Velocity differences between the Lyman- α emission line, interstellar absorption lines, and near-IR nebular lines for galaxies in the NIRSPEC sample. Each point represents one galaxy; shaded regions show the mean velocity difference \pm standard deviation of the mean for two redshift bins. The value of Spearman’s rank correlation coefficient and its significance are $r_s = 0.16$, $P = 0.19$ and $r_s = -0.197$, $P = 0.03$ for the data in the left and right panels, respectively. The weak apparent correlations of velocity offset with redshift are therefore significant at only the $1-2\sigma$ level.

object NIRSPEC sample of Erb et al. (2005, in preparation), and used the results to help assign systemic redshifts to galaxies when NIRSPEC redshifts were unavailable. Figure 1 shows the observed velocity offsets for the galaxies in the full NIRSPEC sample. The least-squares first-order fits to the data can be written

$$z_{\text{neb}} = z_{\text{Ly}\alpha} - 0.0033 - 0.0050(z_{\text{Ly}\alpha} - 2.7) \quad (1)$$

for galaxies with no detected interstellar absorption lines,

$$z_{\text{neb}} = z_{\text{ISM}} + 0.0022 + 0.0015(z_{\text{ISM}} - 2.7) \quad (2)$$

for galaxies with no detected Lyman- α emission, and

$$z_{\text{neb}} = \bar{z} + 0.070\Delta z - 0.0017 - 0.0010(\bar{z} - 2.7), \quad (3)$$

with $\bar{z} \equiv (z_{\text{Ly}\alpha} + z_{\text{ISM}})/2$, $\Delta z \equiv z_{\text{Ly}\alpha} - z_{\text{ISM}}$, for galaxies with detectable Lyman- α emission and interstellar absorption. The rms scatter around the three relationships is $\sigma_z = 0.0027$, 0.0033 , 0.0024 , respectively. In each equation the final term accounts for the weak apparent trend of smaller velocity offsets at lower redshifts. Figure 2 shows the expected error distributions for the galaxies that lack near-IR nebular redshifts, calculated by combining the observed error distributions for equations 1, 2, and 3 after weighting by the number of galaxies in each class (233 with Lyman- α emission only, 425 with interstellar absorption only, 296 with both). For comparison, repeated observations of galaxies in the NIRSPEC sample suggest that these galaxies’ redshifts have a random uncertainty of 60 km s^{-1} .

The criteria used to select galaxies for spectroscopy were irregular. We favored objects with $23 < \mathcal{R} < 24.5$ and objects near any known QSOs, and strongly disfavored objects far from the field centers. Near QSOs we often observed objects whose colors satisfied any of the

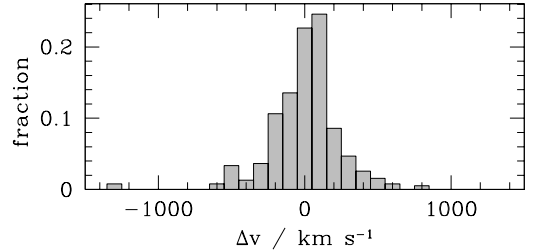


FIG. 2.— Estimated histogram of velocity errors $\Delta v \equiv v_{\text{est}} - v_{\text{true}}$ for galaxies without near-IR nebular redshifts.

U_nGR selection criteria of Steidel et al. (2003) or Adelberger et al. (2004). Far from QSOs our spectroscopic selection tended to be prejudiced towards one or the other color-selection criterion, “BX/BM” or “LBG,” depending on the field. This haphazard approach imposes a complicated selection bias on our data. Rather than try to correct it with elaborate simulations, we restrict our analysis to quantities that are not affected by irregular angular sampling or the assumed redshift selection function. Further details of the galaxy observations can be found in Steidel et al. (2003; 2004) and Erb et al. (2005, in preparation).

The QSO spectra we analyzed were obtained between 1996 and 2003 with either the HIRES echelle spectrograph (Vogt et al. 1994) or the ESI echellette (Sheinis et al. 2000) on the Keck I and II telescopes. The HIRES spectra were reduced using the standard procedures of Tom Barlow’s Makee package. The ESI spectra were reduced with the “Dukee” suite of custom IRAF scripts and C programs written by KLA and M. Hunt. The shape of the continuum was removed from the QSO spectra interactively by fitting a high-order (~ 30) b-spline to regions of the spectra that appeared to be free from absorption. CIV absorption systems in the QSO spectra were identified interactively by scanning for absorption doublets with the right wavelength spacing. Column densities were estimated by fitting each doublet’s absorption profile with two Gaussians in optical depth. This is equivalent to Voigt-profile fitting at the low (i.e., undamped) column-densities of interest to us. Occasionally the velocity profiles were unresolved in our spectra. If this happened and the doublet ratio suggested that the lines were saturated, we obtained a crude estimate of column density from the weaker line only. Otherwise both lines were used. See Adelberger et al. (2003) for further details. Our ability to detect CIV systems depended on the quality of the QSO spectrum. Table 2 lists the minimum detected CIV column density in each QSO’s spectrum. This should be roughly equal to the spectrum’s CIV detection limit.

Figure 3 shows the redshift distributions of the different objects in our sample.

3. GALAXIES’ GASEOUS ENVELOPES

Numerous authors have noticed that the interstellar absorption lines in high-redshift galaxies’ spectra tend to be blueshifted, presumably because they are produced by outflowing gas (e.g., Franx et al. 1997; Pettini et al. 1998, 2001; Frye, Broadhurst, & Benítez 2002; Shapley

TABLE 2. OBSERVED QSOs

QSO	Field	$\alpha(2000)$	$\delta(2000)$	z	G_{AB}^a	n_{CIV}^b	$\log(N_{CIV}^{\min})^c$
PKS0201+113 ^d	Q0201	02 ^h 03 ^m 46.7 ^s	11°34'45''	3.610	20.1	0	-
LBQS0256-0000	Q0256	02 ^h 59 ^m 05.6 ^s	00°11'22''	3.324	18.0	32	12.02
LBQS0302-0019	Q0302	03 ^h 04 ^m 49.9 ^s	-00°08'13''	3.267	17.8	46	12.03
FBQS J0933+2845	Q0933	09 ^h 33 ^m 37.3 ^s	28°45'32''	3.401	18.8	34	12.00
Q1305kkc9	Q1305	13 ^h 07 ^m 42.7 ^s	29°19'36''	2.462	21.3	7	13.56
Q1305kkc16	Q1305	13 ^h 08 ^m 06.1 ^s	29°22'39''	2.526	20.9	4	13.03
Q1305kkc22	Q1305	13 ^h 08 ^m 11.9 ^s	29°25'13''	2.979	19.0	16	13.02
Q1422+2309	Q1422	14 ^h 24 ^m 38.1 ^s	22°56'01''	3.515	16.5	74	11.81
Q1422+2309b	Q1422	14 ^h 24 ^m 40.6 ^s	22°55'43''	3.084	23.4	3	13.45
Q1623kp76	Q1623	16 ^h 25 ^m 48.1 ^s	26°44'33''	2.246	18.5	13	12.72
Q1623kp77	Q1623	16 ^h 25 ^m 48.8 ^s	26°46'59''	2.529	16.5	41	12.03
Q1623kp78	Q1623	16 ^h 25 ^m 57.4 ^s	26°44'49''	2.578	19.0	47	12.14
Q1623kp79	Q1623	16 ^h 26 ^m 06.2 ^s	26°50'33''	2.180	19.2	12	12.99
Q1623BX234	Q1623	16 ^h 25 ^m 33.7 ^s	26°53'44''	2.464	19.5	4	14.06
Q1623BX603	Q1623	16 ^h 26 ^m 02.4 ^s	26°43'39''	2.529	20.5	8	13.32
HS1700+6416	Q1700	17 ^h 01 ^m 00.6 ^s	64°12'09''	2.717	16.0	57	11.71
Q2233+136	Q2233	22 ^h 36 ^m 27.2 ^s	13°57'13''	3.209	18.7	25	12.09
Q2342+125	Q2343	23 ^h 45 ^m 22.8 ^s	12°45'47''	2.497	18.2	9	12.57
Q2343+125	Q2343	23 ^h 46 ^m 28.3 ^s	12°48'58''	2.579	17.0	38	12.25
Q2344+125	Q2343	23 ^h 46 ^m 46.1 ^s	12°45'27''	2.785	17.5	44	12.33
Q2343BX415	Q2343	23 ^h 46 ^m 25.4 ^s	12°47'44''	2.578	20.3	19	13.22
Q2345+000	Q2346	23 ^h 48 ^m 25.4 ^s	00°20'41''	2.652	19.7	3	13.31
SSA22d13	SSA22a	22 ^h 17 ^m 22.3 ^s	00°16'41''	3.343	21.6	6	13.22

^aQSO magnitude; numbers are unreliable brighter than our saturation magnitude $G \sim 18$

^bNumber of detected CIV systems

^cLog of the minimum column density (in cm^{-2}) among the detected CIV systems

^dCIV absorber catalog not constructed owing to gaps in our echelle spectrum

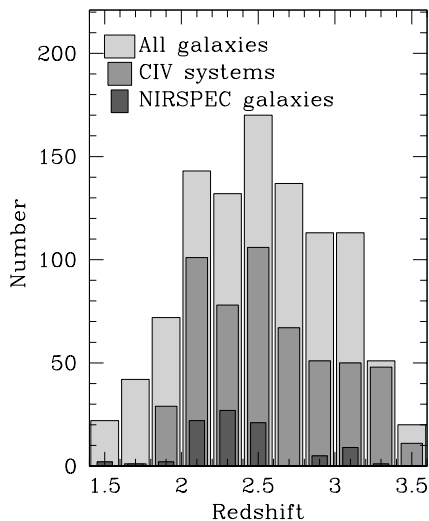


FIG. 3.— Redshift distributions for different objects in our sample.

et al. 2003; Erb et al. 2004). Little is known, however, about how far the outflowing gas might propagate. This section shows that the absorbing material often lies at radii approaching 80 proper kpc and that weaker lines can be detected much farther away. It does not clearly show, however, that the absorbing material detected at large radii is part of an outflow. Other scenarios are considered in §§ 4 and 8.

3.1. Radii $r \lesssim 80$ proper kpc

A ~ 40 kpc radius for galaxies' strongly absorbing material is implied by the presence of foreground galaxies' absorption lines in the spectra of nearby background galaxies. The left panel of Figure 4 illustrates the idea. The right panel shows one example from our survey. Two galaxies with redshifts $z = 1.60$, $z = 2.17$ and angular separation $\theta = 2''$ were placed on the same slit on one of our multislit masks. Light from the background galaxy passed within 17 proper kpc of the foreground galaxy as it traveled towards earth, and this was close enough for the foreground galaxy's absorption lines to be imprinted in its spectrum. The absorbing material must therefore have a radius of at least 17 kpc.

Similar absorption lines are observed in galaxy pairs with impact parameters of up to 40 kpc, but the absorption weakens significantly at greater separations. This can be seen by measuring the dependence on angular separation θ of the mean absorption produced by foreground galaxies. We calculated the strength of the mean absorption in two bins of angular separation. For each bin, we identified all the galaxy pairs in our sample (18 for $1'' < \theta < 5''$, 64 for $5'' < \theta < 10''$; $10''$ corresponds to 81 proper kpc at $z = 2.5$ for a cosmology with $\Omega_M = 0.3$, $\Omega_\Lambda = 0.7$, $h = 0.7$), collected the background spectra, masked parts of the spectra that were contaminated by sky lines or by any of the background galaxy's ten strongest spectral features⁴, shifted each spectrum into the rest-frame of its foreground galaxy,

⁴ Ly β /OVI, Ly α , SiII λ 1260, OI λ 1302, CII λ 1335, SiIV λ 1398, SiII λ 1527, CIV λ 1549, FeII λ 1608, AlII λ 1671

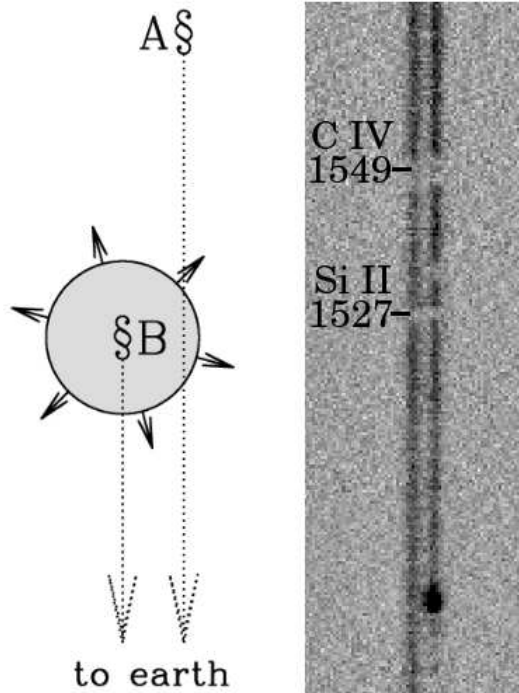


FIG. 4.— Left: Schematic view of galaxy/galaxy absorption. A foreground galaxy, B , is surrounded by a gaseous envelope that may be expanding. Light from the background galaxy, A , passes through this envelope and is imprinted with absorption lines. (A may have an expanding envelope of its own but this is suppressed for simplicity.) Right: Example LRIS spectra of a galaxy pair with $2''$ separation and redshifts $z = 1.61, 2.17$. Spatial position varies along the x axis and wavelength increases towards higher y . The Lyman- α emission line of the higher redshift object is visible at the bottom of the rightmost spectrum. The gas associated with the lower redshift object, on the left, produces absorption lines (labeled) in the spectra of both objects. Its radius must therefore exceed 17 kpc (i.e., $2''$ at $z = 1.61$).

spline-interpolated the rest-frame spectra onto common abscissae, removed the shape of the continuum by forcing each spectrum to have a constant 140\AA running-average flux, and averaged the spectra together with inverse-variance weighting after first rejecting the highest and lowest 10% of the flux values at each output wavelength. Finally we restored a realistic continuum shape by multiplying the resulting spectrum by the mean running-average continuum shape of the sample.

Figure 5 shows the result. The strength of the interstellar CIV absorption line appears roughly constant for $\theta \lesssim 5''$ (~ 40 proper kpc at $z = 2.2$) but drops sharply afterwards.⁵ Chen, Lanzetta, & Webb (2001) found similar results at lower redshifts. It would be wrong to conclude from Figure 5, however, that the observed CIV absorption at $5'' < \theta < 10''$ is weak to the point of insignificance. The estimated rest-frame equivalent width of the absorption, $W_0(\text{doublet}) \sim 0.7\text{\AA}$ (i.e., $W_0(1548) \gtrsim 0.4\text{\AA}$, or $N_{\text{CIV}} \gtrsim 10^{14} \text{ cm}^{-2}$), is large by intergalactic standards. According to Steidel (1990), only 1.2 ± 0.4 CIV systems with $W_0(1548) > 0.4\text{\AA}$ are found per unit redshift at $2 \lesssim z \lesssim 3$. Since our color-selection criteria find

⁵ Note that part of the CIV feature in the top panel of Figure 5 is stellar P-Cygni absorption.

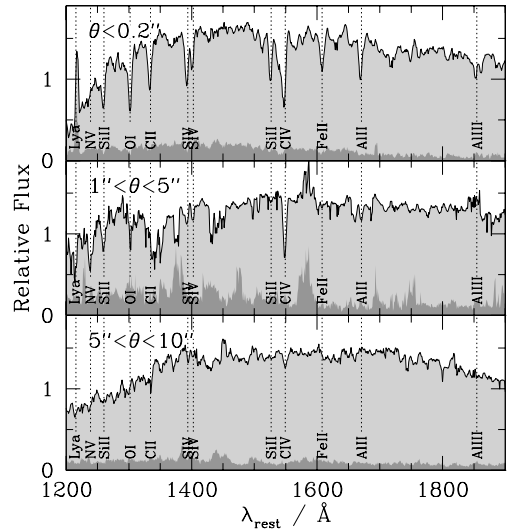


FIG. 5.— Mean gas absorption as a function of galactic impact parameter. Top panel: mean spectrum of the foreground galaxies in pairs with angular separation $1'' < \theta < 5''$ ($8 \lesssim b \lesssim 40$ proper kpc). Their absorption lines are sensitive to the gas density at impact parameters smaller than their half-light radii, i.e., $\theta \lesssim 0.2''$. The names of different absorption and emission lines are indicated. The darker shaded region at the bottom of the panel is the bootstrap error spectrum, estimated by recalculating the mean spectrum for random ensembles of foreground galaxy spectra. Middle panel: mean absorption observed in the spectra of the background galaxy at the redshift of the foreground galaxy. This panel is noisier, owing to our masking of interstellar features and (at bluer wavelengths) to Lyman- α forest absorption in the spectra of the background galaxies. Apparent features should be viewed skeptically. Comparison to the error spectrum shows that some of them are not significant (e.g., absorption near 1375\AA , emission near 1580\AA). Bottom panel: similar to the middle panel, but this is the mean absorption produced in the spectra of background galaxies with angular separation $5'' < \theta < 10''$ ($40 \lesssim b \lesssim 80$ proper kpc).

9 galaxies per arcmin² per unit z at the same redshifts (e.g., Steidel et al. 2004), they would account for the majority of all CIV-systems with $W_0(1548) > 0.4\text{\AA}$ if each galaxy produced absorption with $W_0(1548) > 0.4\text{\AA}$ out to $\theta = 10'' = 0.167'$: $9 \times \pi(0.167')^2 \simeq 0.8$ CIV absorbers per unit redshift. In fact, as we will see below (Figure 8), only about half of the galaxies within $10''$ (~ 80 kpc) are associated with CIV absorption so strong. This implies that the galaxies in our sample can account for roughly one-third of CIV lines with $W_0(1548) > 0.4\text{\AA}$. Galaxies missed by our UV-color-selection techniques could easily account for the remainder.

The large equivalent width $W_0(\text{doublet}) \simeq 2.7\text{\AA}$ of the absorption at $\theta < 5''$ has an interesting implication. CIV can attain so high an equivalent width only if peculiar velocities spread the absorption over a large range of wavelengths. The minimum velocity spread is $\Delta v = 260 \text{ km s}^{-1}$, but this assumes a contrived situation where each line in the doublet is saturated and has a boxcar (ie, maximally compact) absorption profile. In realistic situations the CIV absorption will have complicated substructure (e.g., Pettini et al. 2002) and a significantly larger velocity spread will be required to produce $W_0(\text{doublet}) \simeq 2.7\text{\AA}$. Our lower limit to the velocity spread ($\Delta v = 260 \text{ km s}^{-1}$) is smaller than the likely es-

cape velocity at 40 kpc from a galaxy with $M \sim 10^{12} M_{\odot}$ (e.g., Adelberger et al. 2004), but it nevertheless shows that significant chaotic motions in the gas extend to large radii.

Further evidence comes from one of the two cases in our survey where a foreground galaxy lies within $15''$ of the QSO sightline and the QSO is lensed into two detectable components with $\sim 1''$ separation. In this case, shown in the left panel of Figure 6, the galaxy’s gas produces significantly different absorption profiles in the spectra of the two QSO components. The implied substructure on half-kpc scales would be erased by thermal motions in a few dozen Myr if it were not maintained somehow. The gas along the two sightlines might have supersonic relative motions or might be gravitationally confined in two separate mini-halos. Substructure of this sort is rare in the low-density intergalactic medium (Rauch et al. 2001b) but common among CIV systems (Rauch, Sargent, & Barlow 2001a).

3.2. Radii $r \gtrsim 80$ proper kpc

Although the metal absorption lines continue to weaken beyond $r \sim 80$ kpc, they are not always absent. High signal-to-noise QSO spectra reveal that absorbing gas extends out to 100-200 proper kpc in at least some cases. Figure 7 shows three. Absorption from metal-enriched, multiphase gas is detected in each. (See §§ 2.5.13 and 2.5.15 of Simcoe et al. 2002 for a discussion of the physical conditions in two of these absorption systems.)

These three cases are not typical, but nor are they extraordinarily rare. Figure 8 shows the total detected CIV column density within $100\text{--}500 \text{ km s}^{-1}$ of the 29 galaxies in our NIRSPEC sample that lie within $1.0h^{-1}$ projected comoving Mpc of a QSO with detected CIV⁶. The CIV column densities of the three examples in Figure 7 are the second, third, and seventh highest in this 29 object sample.

One way to show that the detected metals are associated with a nearby galaxy, and are not chance alignments, is to measure the galaxy-CIV correlation strength $\bar{\xi}_{\text{gc}}$ on small spatial scales. As pointed out by Adelberger et al. (2003), $\bar{\xi}_{\text{gc}}$ cannot easily exceed $\bar{\xi}_{\text{gg}}^{1/2} \bar{\xi}_{\text{cc}}^{1/2}$, the geometric mean of the galaxy-galaxy and CIV-CIV clustering strengths, unless the existence of galaxies affects (or is affected by) the presence of nearby CIV systems. Since ξ_{gg} and ξ_{cc} are roughly equal (Quashnock & van den Berk 1998; Adelberger et al. 2003), a value of $\bar{\xi}_{\text{gc}}/\bar{\xi}_{\text{gg}}$ significantly greater than unity on small scales would imply a direct relationship between the galaxies and CIV systems.

We estimated $\bar{\xi}_{\text{gc}}/\bar{\xi}_{\text{gg}}$ with the following approach. For each CIV system, we counted the observed number n_i of NIRSPEC galaxies with velocity separation $|\Delta v| < v_{\text{max}}$ and transverse separation $R_{\text{min}} < R < R_{\text{max}}$. Call these galaxies the CIV system’s neighbors. (We took $v_{\text{max}} = 500 \text{ km s}^{-1}$ and $R_{\text{max}} \lesssim 1h^{-1}$ comoving Mpc, since these are roughly the maximum separations expected for a galaxy’s ejecta.) Given the galaxies’ known angular distances to the QSO, the expected number of

neighbors is (see, e.g., Adelberger 2005)

$$\bar{n}_i = \sum_j^{\text{galaxies}} \frac{\int_{z_i - \Delta z}^{z_i + \Delta z} dz P(z) [1 + \xi(\mathbf{r}_{ij})]}{\int_0^{\infty} dz P(z) [1 + \xi(\mathbf{r}_{ij})]} \quad (4)$$

where the sum runs over all NIRSPEC galaxies in the QSO’s field, Δz is the redshift difference corresponding to v_{max} , $P(z)$ is the survey selection function normalized so that $\int_0^{\infty} P(z) dz = 1$, ξ is the correlation function, and \mathbf{r}_{ij} is the distance between the CIV-system at redshift z_i and a point at redshift z with the galaxy’s angular separation θ_j . The number of neighbors expected in the absence of clustering, \bar{n}_i^0 , can be calculated from equation 4 with $\xi = 0$, allowing us to estimate the galaxy-CIV clustering strength through $\bar{\xi}_{\text{gc}} = -1 + \sum_i n_i / \sum_i \bar{n}_i^0$. This is the mean value of ξ_{gc} within a complicated volume consisting of many parallel skewers of length $2v_{\text{max}}$. To estimate the mean value of the galaxy-galaxy correlation function within the same volume, we inserted $\xi = \xi_{\text{gg}} = (r/4h^{-1} \text{ comoving Mpc})^{-1.6}$ (e.g., Adelberger et al. 2005) into equation 4, integrated numerically, called the result \bar{n}_i^{gg} , and used the formula $\bar{\xi}_{\text{gg}} = -1 + \sum_i \bar{n}_i^{\text{gg}} / \sum_i \bar{n}_i^0$. The estimates of $\bar{\xi}_{\text{gc}}$ and $\bar{\xi}_{\text{gg}}$ do not depend on any assumptions about the redshift selection function of the CIV systems or the angular selection function of the galaxies. This is fortunate since neither is well known.

Figure 9 shows $\bar{\xi}_{\text{gc}}/\bar{\xi}_{\text{gg}}$ for $R_{\text{min}}, R_{\text{max}} = 0, 0.4$ and $0.4, 1.0h^{-1}$ comoving Mpc. Our data are consistent with no increase in $\bar{\xi}_{\text{gc}}$ over $\bar{\xi}_{\text{gg}}$ on small scales. They are therefore consistent with the idea that galaxies and CIV-systems are spatially correlated only because they trace the same large-scale structure. We cannot rule out a more direct association, however, both because the error bars in Figure 9 are large and because the statistical test itself can detect only the strongest direct associations of galaxies and CIV-systems.

We conclude this subsection by emphasizing one of its corollaries: many of the strongest intergalactic absorption lines are produced by material that lies close to star-forming galaxies. Figure 10 helps illustrate the point. The figure’s vertical lines mark the redshifts of strong CIV and OVI absorption in the spectrum of HS1700+6416.⁷ Circles mark the positions of galaxies near the QSO sightline. Small regions with a wealth of galaxies and intergalactic metals tend to be surrounded by vacant expanses with neither. The correspondence between star-forming galaxies and strong metal lines is not perfect, but one could do worse than assume that the presence of one implies the presence of the other.

4. THE GALAXY-CIV CROSS-CORRELATION FUNCTION

The previous section discussed the relationship between galaxies and metal absorption lines for a small number of specific cases. This section takes a more systematic approach, calculating the cross-correlation function between the positions of galaxies and CIV absorption systems.

4.1. Large scales

⁷ The redshifts of OVI absorption were taken from Simcoe et al. (2002); none of the other QSOs in our sample were analyzed by them, and we have not attempted to find OVI systems ourselves.

⁶ A small fraction of our QSOs were too faint to allow us to detect significant numbers of CIV systems.

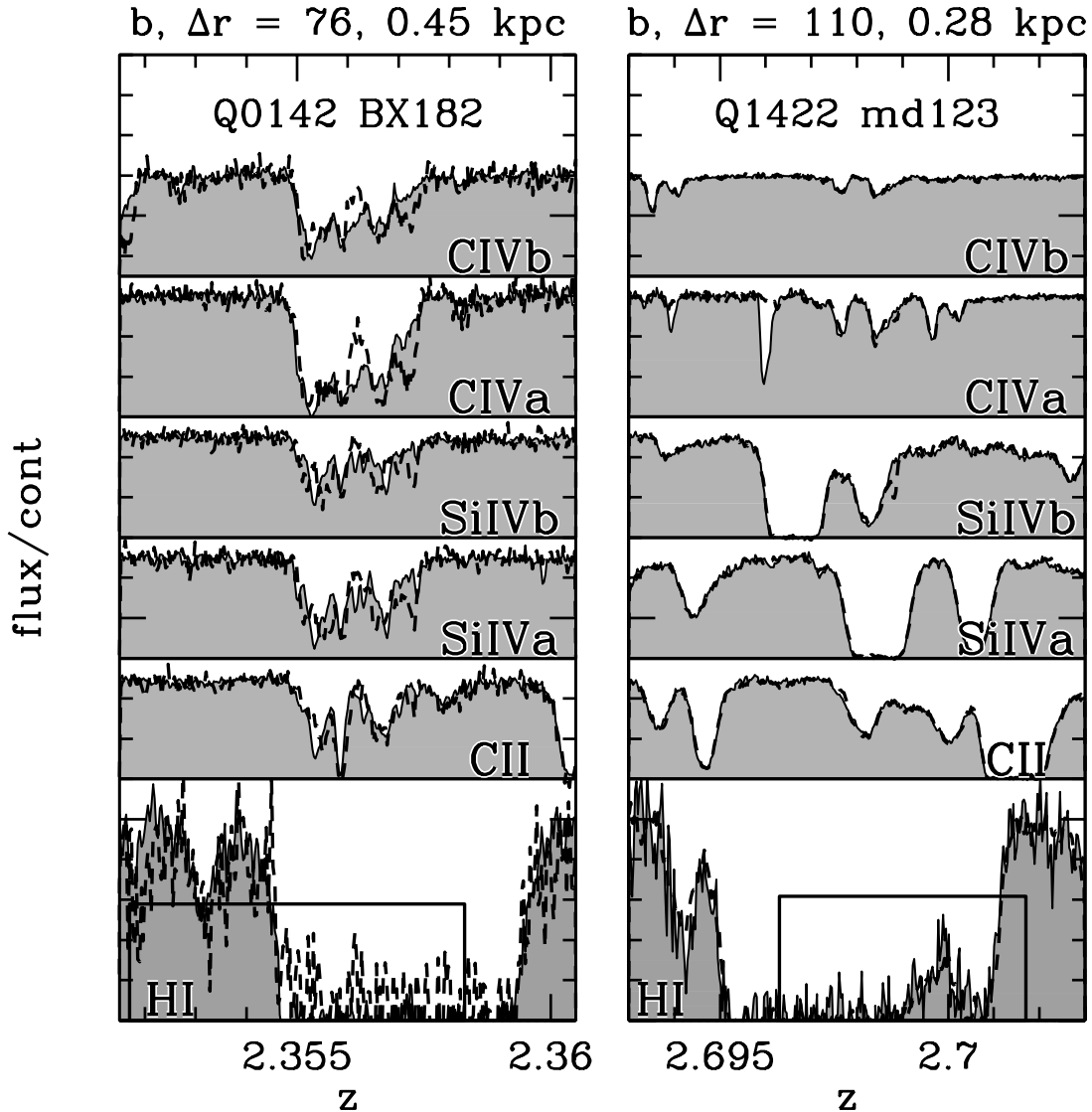


FIG. 6.— Substructure in metal-enriched gas near galaxies. Each panel is for a single galaxy that lies within $15''$ of a background QSO that is lensed into two components with $\sim 1''$ separation. The proper projected distance from galaxy to QSO sightline (b) and proper projected separation of the two QSO components (Δr) are indicated above the panels; Δr is taken from Rauch et al. 2001a. The $\pm 1\sigma$ range of the galaxy’s redshift is indicated by the rectangle at the bottom of each figure. The Lyman- α and metal-line absorption near the galaxy’s redshift is shown in the stacked spectral segments, which are drawn shaded for one QSO component and dashed for the other. Significant differences are apparent in the left-hand panel but not the right. (In the right hand panel, the Lyman- α forest falls in the same part of the QSO spectrum as the SiIV and CII absorption lines, making it difficult to determine if these features are present or absent.) The recently obtained galaxy redshifts near Q0142-100 have been used only for this plot, and this field has consequently been omitted from Tables 1 and 2.

Our approach on large spatial scales is similar to that of Adelberger (2005): we assume that the cross-correlation function has the form $\xi(r) = (r/r_0)^{-1.6}$ (e.g., Adelberger et al. 2003); count the number $n_{\text{obs}}(0, \ell)$ of galaxy-CIV pairs in our sample that have $\Delta\theta < 300''$, $|\Delta Z| < \ell$ for $\ell = 20, 40h^{-1}$ comoving Mpc⁸; calculate the expectation value of $n_{\text{obs}}(0, 20)/n_{\text{obs}}(0, 40)$ as a function of r_0 with

⁸ ΔZ is the comoving separation in the redshift direction between the galaxy and CIV system; i.e., it is the comoving distance between the galaxy’s redshift z_g and the CIV system’s z_c .

the equation (Adelberger et al. 2005; Adelberger 2005)

$$\left\langle \frac{n_{\text{obs}}(0, \ell)}{n_{\text{obs}}(0, 2\ell)} \right\rangle \simeq \frac{\sum_{i,j} \int_0^\ell dZ [1 + \xi(R_{ij}, Z)]}{\sum_{i,j} \int_0^{2\ell} dZ [1 + \xi(R_{ij}, Z)]}, \quad (5)$$

where $\xi(R, Z) \equiv \xi[(R^2 + Z^2)^{1/2}]$, $R_{ij} \equiv (1 + z_i)D_A(z_i)\theta_{ij}$, $D_A(z)$ is the angular diameter distance, and the summation is over all galaxies (i) and CIV-systems (j); and finally take as our best estimate of r_0 the value that makes the right-hand side of equation 5 equal the observed ratio $n_{\text{obs}}(0, 20)/n_{\text{obs}}(0, 40)$. As discussed in Adelberger et al. (2005) and Adelberger (2005), the resulting estimate of r_0 is insensitive to angular selection effects and only weakly dependent on the assumed shape of the selection

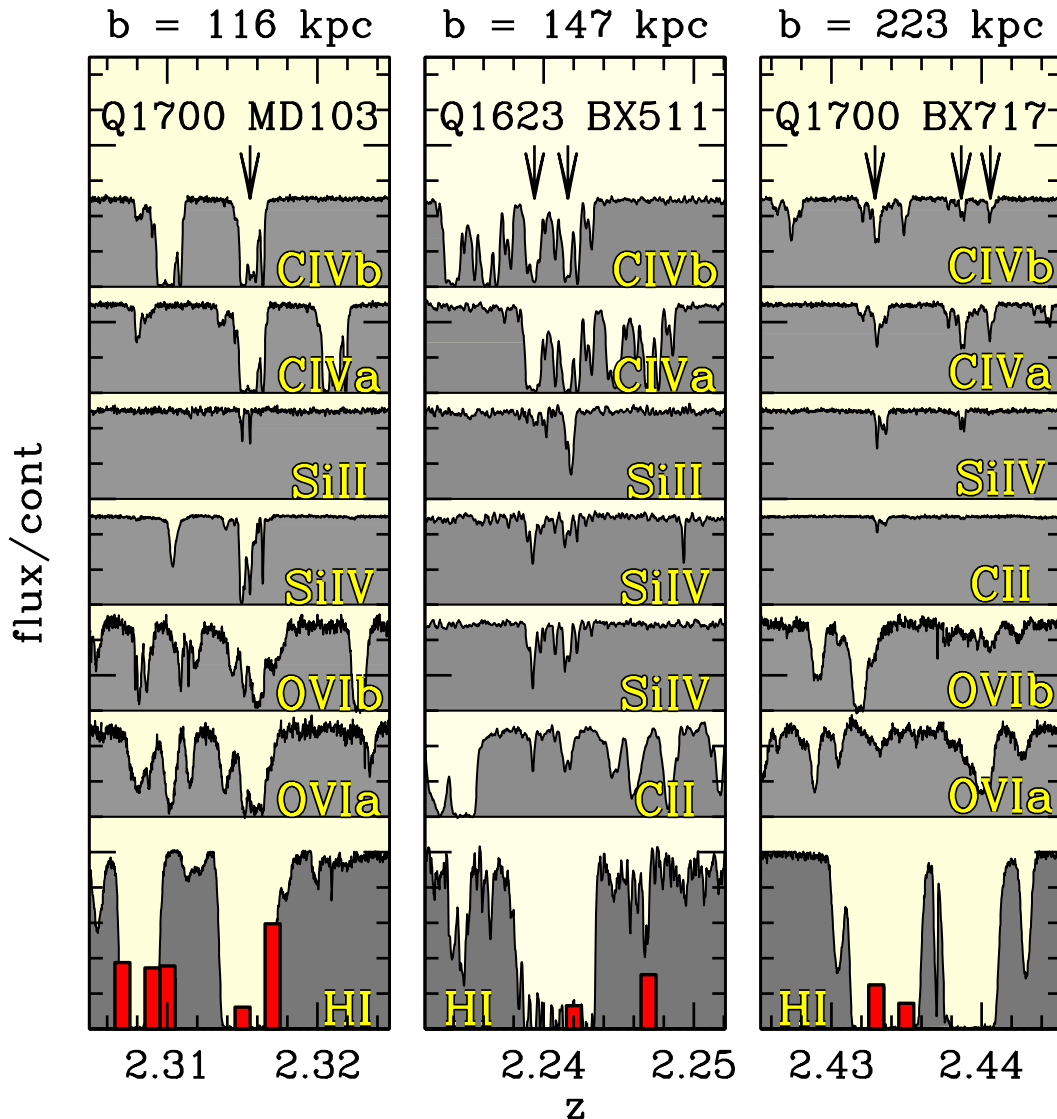


FIG. 7.— Absorption lines in QSO spectra at the redshifts of nearby galaxies. Each of the three panels (left, middle, right) is for a single galaxy, with proper impact parameter indicated above. The galaxy’s redshift, measured with NIRSPEC, is marked by the short bar in the center of the panel. The width of the bar, $\pm 60 \text{ km s}^{-1}$, is equal to the redshift’s 1σ uncertainty. The redshifts of neighboring galaxies are indicated with the other bars. The neighboring galaxies were not observed with NIRSPEC and so their redshifts are more uncertain, with $\pm 1\sigma$ limits roughly 5 times broader than the bars. The bars’ heights are proportional to the galaxies’ impact parameters. The HI absorption near the galaxy’s redshift is shown at the bottom of the panel. Accompanying metal-line absorption, if any, is shown above. Redshifts of detected metal absorption are marked with downward pointing arrows near the top of the panel. The velocity range shown in each panel, roughly $\pm 900 \text{ km s}^{-1}$, is small enough that absorption lines visible anywhere in a panel could conceivably be produced by gas flowing out of the galaxy in the middle. Some of the lines (e.g., OVI, CII) fall within the Lyman- α forest, and observed absorption can be attributed to them with confidence only if other metal-lines are present at the same redshift.

function—two significant advantages given the irregular selection criteria we employed (§ 2).

Figure 11 shows the estimated cross-correlation length as a function of the CIV system’s column density. To estimate the uncertainty, we broke our galaxy and CIV catalogs into many smaller sub-catalogs by rejecting a random fraction $p = 0.5\text{--}0.8$ of the sources, observed how the dispersion in best-fit r_0 among the sub-catalogs depended on the number of objects in the catalogs, and extrapolated to the full catalog sizes. This accounts for random uncertainties but not completely for cosmic variance.

Also drawn in Figure 11 is the 1σ confidence interval for the galaxy-galaxy correlation length at similar redshifts, taken from Adelberger et al. (2005). The good agreement of the galaxy-galaxy and galaxy-CIV correlation lengths for $N_{\text{CIV}} \gtrsim 10^{12.5} \text{ cm}^{-2}$ shows that bright star-forming galaxies and stronger CIV systems have similar spatial distributions, reinforcing the idea (§ 3) that they are often the same objects. Adelberger et al. (2003) reached a similar conclusion.

4.2. Small Scales

As mentioned above, an observed spatial association of galaxies and CIV systems does not by itself imply

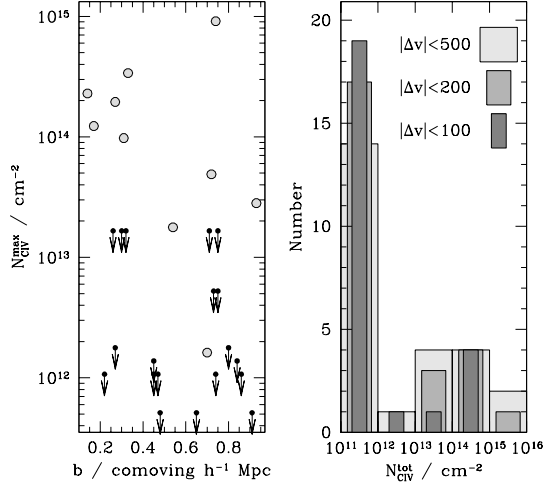


FIG. 8.— Left panel: Column density of the strongest detected CIV system within $\pm 200 \text{ km s}^{-1}$ of the galaxy as a function of galaxy impact parameter b . Large points show detections. Small points with arrows show upper limits. We assumed that the upper limit would be equal to the column density of the weakest detected CIV system in the QSO’s spectrum. Right panel: Distribution of the total detected CIV column density near galaxies that lie within $1 h^{-1}$ comoving Mpc of the QSO sightline. The total column density was calculated by summing the column densities of all CIV systems within 100, 200, or 500 km s^{-1} of the galaxy’s redshift. For simplicity, the non-detections are all placed in the bin with $N_{\text{CIV}} < 10^{12} \text{ cm}^{-2}$. This panel provides some indication of how the left panel would change for velocity limits other than $\pm 200 \text{ km s}^{-1}$. The same galaxies were used in both panels; all have precise (i.e., near-IR nebular) redshifts.

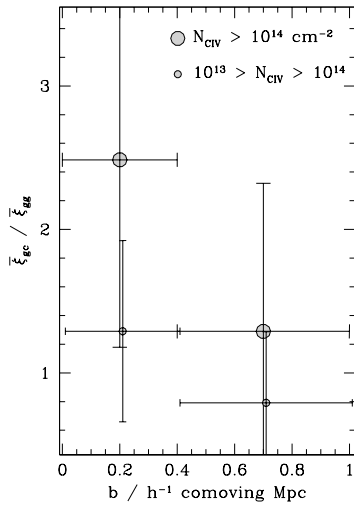


FIG. 9.— Estimated ratio of mean galaxy-CIV and galaxy-galaxy clustering strength as a function of galaxy impact parameter b . The correlation functions are averaged over $\pm 500 \text{ km s}^{-1}$ for each galaxy. Points show the ratios for CIV systems in two column-density ranges, as indicated. The 1σ error bars were calculated under the assumption that the variance in the number of pairs N is $\text{Var}(N) \simeq 1.56N^{1.24}$, an approximation that Adelberger (2005) found to be accurate for galaxy pair counts in the Lyman-break survey.

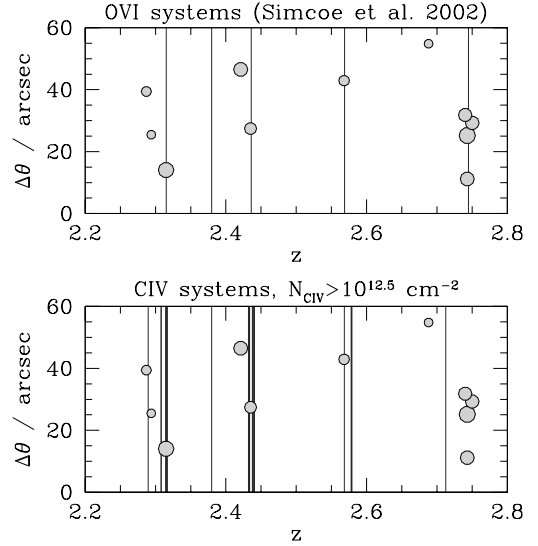


FIG. 10.— Redshifts of galaxies near the sightline to QSO HS1700+6416 compared to the redshifts of CIV and OVI absorption systems in the QSO’s spectrum. Circles mark galaxy redshifts and impact parameters. The area of each circle is proportional to the galaxy’s apparent luminosity in the \mathcal{R} band. Vertical lines mark the redshifts of OVI and CIV absorption. Thicker lines in the CIV panel mark systems with multiple components. OVI absorption redshifts are taken from Simcoe, Sargent, & Rauch (2002). The absorption line catalogs are reasonably complete down to their limiting equivalent widths, but, owing to imperfect color-selection criteria and limited time for follow-up spectroscopy, it is unlikely that the galaxy catalogs contain more than half of the galaxies brighter than $\mathcal{R} = 25.5$ at these redshifts. (We obtained redshifts for 15 of the 20 photometric candidates within $60''$ of the sightline to this QSO, so most of the expected incompleteness is due to our color-selection criteria. See, e.g., Adelberger et al. 2004.)

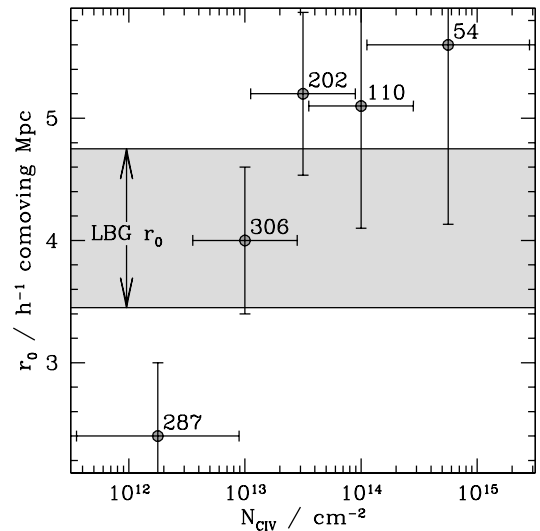


FIG. 11.— Galaxy-CIV cross-correlation length r_0 as a function of CIV column density. Circles show the measurements of section 4. The number near each point indicates the number of CIV systems with column densities in the bin’s range. The shaded region in the background shows the galaxy-galaxy correlation length r_0 appropriate to this sample (Adelberger et al. 2005).

that the detected metals are part of a galactic superwind. Many other processes could place metals near galaxies. One way to learn about the relationship between intergalactic CIV and nearby galaxies is to look for anisotropies on small scales in the redshift-space galaxy-CIV correlation function. Since these anisotropies are produced by peculiar velocities, they should reveal whether the CIV tends to be falling towards, flowing away from, or orbiting around the nearest galaxy. Figure 12 shows the observed spatial separation of every galaxy-CIV pair in our NIRSPEC sample that had comoving redshift separation $|\Delta Z| < 10h^{-1}$ Mpc and comoving angular separation $b < 1h^{-1}$ Mpc. Vertical lines mark the impact parameters of each galaxy-QSO pair. Circles on these lines show the velocities (relative to the nearby galaxy) of any detected CIV absorption in the QSO's spectrum. Only galaxies with NIRSPEC redshifts are shown in the plot, since precise redshifts are crucial to our arguments.

The peculiar velocities of CIV systems relative to galaxies can be estimated roughly from this plot as follows. The expected number of galaxy-CIV pairs with impact parameter b and radial separation $|\Delta Z| < Z_1$ is proportional to $[1 + \bar{\xi}(b, < Z_1)]Z_1$, where

$$\bar{\xi}(b, < Z_1) \equiv \frac{1}{Z_1} \int_0^{Z_1} dZ \xi(b, Z) \quad (6)$$

and $\xi(b, Z)$ is the galaxy-CIV correlation function. On average, then, half of the plot's galaxies with impact parameter b should have comoving redshift separation $|\Delta Z| < Z_{1/2}(b)$ with

$$Z_{1/2}(b) = \frac{Z_{\max}}{2} \frac{1 + \bar{\xi}(b, < Z_{\max})}{1 + \bar{\xi}(b, < Z_{1/2})} \quad (7)$$

where $|\Delta Z| < Z_{\max}$ is the range of redshift separations shown on the plot. If peculiar velocities were negligible, $\xi(b, Z)$ would be equal to the real-space galaxy-CIV correlation function ξ^r , which must be isotropic in an isotropic universe: $\xi(b, Z) = \xi^r[(b^2 + Z^2)^{1/2}]$. Since $\xi^r(r) = (3.7h^{-1}\text{Mpc}/r)^{1.6}$ is a reasonably good approximation to the real-space correlation function (see Figure 9), one can solve for $Z_{1/2}(b)$ numerically by inserting this correlation function into equations 7 and 6.

The dotted triangular envelope in Figure 12 shows $Z_{1/2}(b)$. Half of the CIV systems would be expected to lie within the dotted envelope in the absence of peculiar velocities. In fact 66 of 81 lie outside. Peculiar velocities appear to be substantial. The observations seem inconsistent with an infall model, since infall tends to compress correlation functions in the redshift direction; it would place more than half of the CIV systems inside the envelope. The random motions of orbiting clouds would move some CIV systems outside the envelope through the finger-of-god effect, but it is unclear if the expected size of the displacements ($\pm 1.4h^{-1}$ comoving Mpc for $\sigma_{1d} = 140 \text{ km s}^{-1}$; e.g., Adelberger et al. 2005) is large enough to account for our observations. The small sample size prevents us from drawing firm conclusions, but outflows moving at several hundred km s^{-1} might become the favored explanation if the correlation function remains so anisotropic as the sample size grows.

5. INTERGALACTIC HI NEAR GALAXIES

After noticing that none of the three galaxies closest to background QSOs in their sample seemed to be associated with strong Lyman- α absorption lines, Adelberger et al. (2003) speculated that superwinds extending to $\sim 0.5h^{-1}$ Mpc might drive most intergalactic hydrogen away from young galaxies. Our larger sample puts this speculation to rest. The top panel of Figure 13 shows the measured transmissivity of every Lyman- α forest pixel⁹ in our QSO spectra that lies within $1h^{-1}$ comoving Mpc of a galaxy with precisely known (i.e., near-IR nebular) redshift. The distances shown on the x -axis are imprecise, because they were calculated from redshift differences under the assumption that peculiar velocities are negligible, but nevertheless it is clear that strong HI absorption is common near the galaxies.

The bottom panel of Figure 13 shows the same data with the pixels grouped by galaxy. Each point marks $\bar{f}_{1\text{Mpc}}$, the mean Lyman- α transmissivity of the pixels within $1h^{-1}$ comoving Mpc of a single galaxy, and the error bar shows the r.m.s. spread among these pixel values. Table 3 lists the impact parameters and redshifts for the galaxies in this figure. Also listed is c , the smoothed mean transmissivity in the QSO's spectrum at the galaxy's redshift, calculated by convolving the continuum-normalized QSO spectrum by a boxcar with width 100\AA and fitting a 2nd-order polynomial to the result.

Figure 14 shows that the mean transmissivity declines monotonically as one approaches a galaxy. This appears inconsistent with the earlier result of Adelberger et al. (2003; dashed circles). The present analysis differs from theirs in three main ways: our redshifts are more precise, our sample is larger, and our galaxies' typical redshift is lower. Each difference could contribute to the change in this plot. The good agreement of the results for the NIRSPEC-only and full samples in Figure 14 suggests that the redshifts' precision might not be primarily responsible for the change. This suspicion is reinforced by our NIRSPEC observations of galaxies in the sample of Adelberger et al. (2003). Although two of their three galaxies with $r < 0.5h^{-1}$ comoving Mpc had redshifts that placed the nebular lines outside of atmospheric windows, the near-IR nebular redshift we obtained for the third confirmed the reported lack of nearby Lyman- α absorption.¹⁰ Another possibility is that genuine evolution from $z \sim 3$ to $z \sim 2$ is partly responsible for the increased absorption near galaxies in this sample. The thought is not absurd: at lower redshifts, galaxies have marginally slower outflows (see Figure 1) and a larger fraction of intergalactic HI absorption is produced by gas in deep potential wells that is more difficult to disrupt. These changes are not enormous, however, and it seems unlikely to us that they would have a dominant effect. The most obvious difference from Adelberger et al. (2003) is the sample size, especially at small separations. The following simple argument suggests that a statistical fluctuation could plausibly be responsible for lack of absorption at $r < 0.5h^{-1}$ comoving Mpc reported

⁹ We excluded pixels within damped Lyman- α systems, within $\Delta z = 0.05$ of the QSO, or within parts of the Lyman- α forest that could be contaminated by Lyman- β absorption from gas at higher redshifts.

¹⁰ though it altered the galaxy's redshift by more than anticipated by Adelberger et al. (2003).

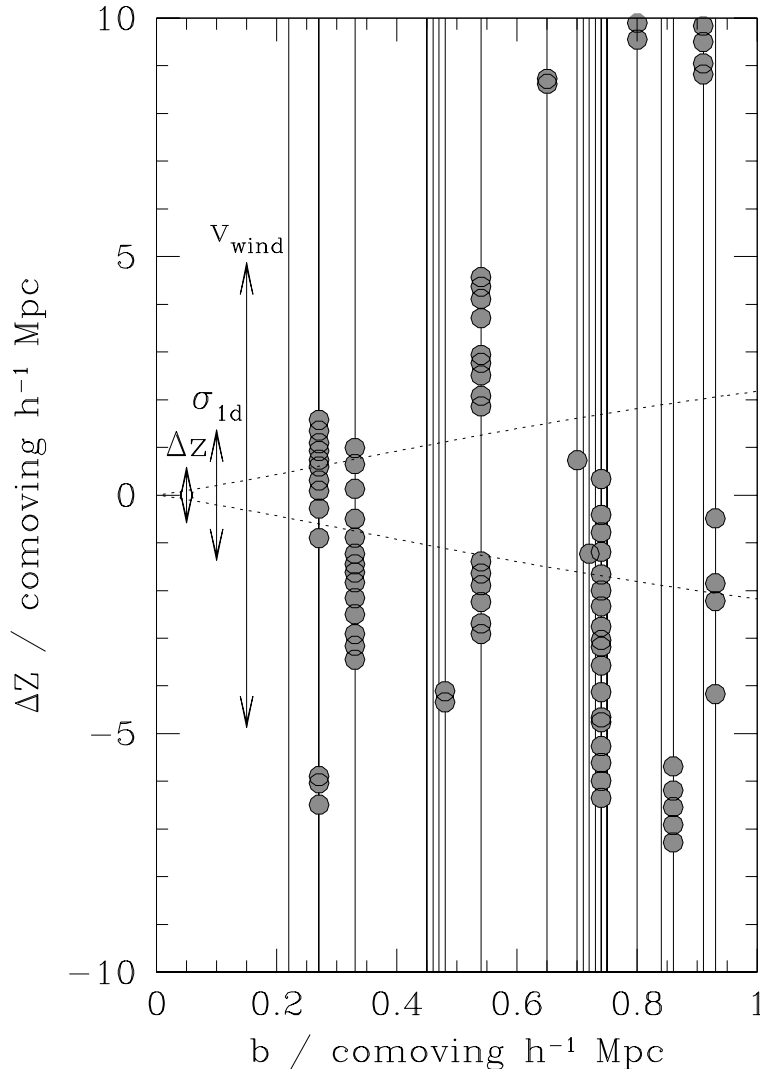


FIG. 12.— Spatial separations of galaxy-CIV pairs in the angular (b) and redshift (ΔZ) direction. Vertical lines show the projected distance between each galaxy in the NIRSPEC sample and its nearest QSO. The QSO spectra allow us to detect any CIV-absorbing gas along these lines. Circles show the actual locations of detected CIV absorption, with one circle at the redshift of each resolved absorption component. In the absence of peculiar velocities, the distribution of CIV systems around galaxies would be spherically symmetric on average and (as a result) half of the circles would be expected to lie inside the dotted triangular envelope (see § 4). In fact 65 of 81 lie outside. The uncertainty in each galaxy-CIV pair’s redshift separation (i.e., in each circle’s vertical position) is too small to account for this ($\pm 1\sigma$ size indicated by two-headed arrow labeled Δz). Peculiar velocities must therefore be substantial. If the CIV systems were orbiting in the galaxy’s halo, their observed redshift separations would be displaced relative to their true separations by a random amount comparable to their galaxy’s velocity dispersion σ_{1d} . The approximate size of $\pm\sigma_{1d}$ (140 km s^{-1}) is indicated by the labeled double-headed arrow. If the CIV were infalling, the CIV systems’ observed (i.e., redshift space) positions would be artificially compressed towards the x axis by an amount comparable to σ_{1d} . If it were flowing outwards, the observed positions would be displaced away from the x axis by an amount that depends on the wind speed. The two-headed arrow labeled v_{wind} shows the approximate size of $\pm 500 \text{ km s}^{-1}$.

by Adelberger et al. (2003). Suppose that half of the galaxies with $r < 0.5h^{-1}$ comoving Mpc are heavily obscured ($f = 0$) and half are unobscured ($f = 1$). This is a rough approximation to the data in the bottom panel of Figure 13. Then the mean and standard deviation of the average transmissivity for a three-object sample would be $\bar{f}_3 = 0.5 \pm 0.29$. Although an observation of $\bar{f}_3 = 1$ superficially seems inconsistent with this scenario, differing by almost 2σ from the expectation $\bar{f}_3 = 0.5$, in fact it should occur one time out of eight. The real world is only vaguely similar to our simple model, but the point

is that large fluctuations occur often in samples drawn from a bimodal underlying distribution. The results in this paper and in Adelberger et al. (2003) are clearly not the same, but they are less inconsistent than one might naively suppose.

In any case, although strong HI absorption is the norm at small separations, we continue to find some galaxies with little absorption. The existence of these galaxies is surprising: one would expect all galaxies to reside in dense regions with significant hydrogen and an elevated neutral fraction from the ρ^2 dependence of the recom-

TABLE 3. GALAXIES WITH IMPACT PARAMETER $b < 1h^{-1}$ COMOVING Mpc^a

b^b	z^c	$\bar{f}_{1\text{Mpc}}^d$	c^e	N_{CIV}^f	Δv_a^g	Δv_e^h	M_*^i	SFR ^j	E^k	Age ^l	τ^m	Galaxy name
0.14	2.181	-	-	14.36	19	x	-	-	-	-	-	Q1623-BX215
0.17	2.175	-	-	14.29	x	x	0.6	14	0.165	1.6	1.0	Q2343-BX429
0.22	2.182	0.27	0.84	x	x	500	1.5	12	0.060	12.8	100	Q1623-BX432
0.26	2.222	-	-	x	-130	419	2.4	15	0.110	16.1	100	Q2343-BX417
0.27	2.243	0.32	0.80	x	-435	x	3.7	21	0.110	1.8	0.5	Q2343-BX587
0.27	2.315	0.00	0.79	14.92	x	x	10.5	19	0.160	4.0	1.0	Q1700-MD103
0.30	2.231	-	-	x	-167	529	1.2	31	0.150	4.0	100	Q2343-BX390
0.31	2.266	-	-	13.99	x	x	-	-	-	-	-	Q2346-BX120
0.32	2.112	-	-	13.28	-270	289	4.4	34	0.195	4.0	2.0	Q2343-BX435
0.33	2.242	0.00	0.75	15.11	x	x	1.2	10	0.180	2.5	1.0	Q1623-BX511
0.45	2.419	0.89	0.83	x	x	x	2.3	5	0.010	6.4	2.0	Q1623-BX449
0.45	2.476	0.90	0.81	x	-130	x	9.7	37	0.165	16.8	20	Q1623-BX522
0.46	2.931	0.98	0.67	-	-382	0	-	-	-	-	-	Q0201-md25
0.47	2.148	0.39	0.83	x	-29	x	8.0	10	0.050	14.3	5.0	Q1623-BX447
0.48	1.968	-	-	-	x	x	1.7	1	0.1	0.8	0.1	Q2346-BX220
0.48	2.294	0.90	0.78	12.81	x	x	2.9	14	0.170	18.0	50	Q1700-MD109
0.54	2.435	0.13	0.79	14.00	x	236	0.7	4	0.005	2.9	1.0	Q1700-BX717
0.65	2.189	0.24	0.77	x	x	x	13.7	9	0.125	27.5	10	Q1700-BX691
0.70	3.039	0.10	0.71	12.21	x	x	-	-	-	-	-	Q2233-MD39
0.71	3.018	0.22	0.59	x	x	x	-	-	-	-	-	SSA22a-C31
0.72	3.099	0.32	0.60	13.69	-278	381	-	-	-	-	-	SSA22a-C35
0.73	2.059	0.77	0.61	x	98	x	9.3	16	0.135	27.5	20	Q1623-BX452
0.74	2.054	0.09	0.78	15.17	-30	511	2.0	2	0	2.5	0.5	Q1623-BX428
0.74	2.407	0.99	0.83	14.12	-70	x	0.1	86	0.270	0.1	0.1	Q1623-BX455
0.75	2.016	0.29	0.56	x	-199	x	0.6	4	0.070	0.5	0.1	Q1623-BX429
0.75	3.066	0.06	0.59	x	x	826	-	-	-	-	-	SSA22a-C39
0.80	2.340	0.83	0.73	x	-323	x	1.2	19	0.110	2.9	2.0	Q2343-BX537
0.84	2.424	0.30	0.81	x	-166	x	9.2	51	0.145	18.0	100	Q1623-BX516
0.86	2.409	0.50	0.83	13.90	-211	598	0.6	92	0.180	0.2	0.1	Q1623-BX376
0.91	2.421	0.98	0.79	x	x	x	3.6	22	0.155	2.9	1.0	Q1700-BX759
0.93	2.174	0.32	0.81	14.26	-151	331	2.6	9	0.010	27.5	100	Q2343-BX660

^aUnobserved quantities are marked “-”; quantities we could not measure owing to noise in the data are marked “x.”

^bComoving impact parameter, h^{-1} Mpc

^cRedshift

^dMean transmissivity of pixels within $1h^{-1}$ comoving Mpc

^eMean transmissivity of random pixels with similar redshifts in the QSO’s spectrum

^fTotal detected CIV column density within 200 km s⁻¹ of the galaxy redshift, cm⁻²

^gVelocity difference between interstellar absorption lines and nebular emission lines, km s⁻¹. Typical uncertainty ~ 200 km s⁻¹.

^hVelocity difference between Lyman- α and nebular emission lines, km s⁻¹. Typical uncertainty ~ 100 km s⁻¹.

ⁱStellar mass, $10^{10}M_{\odot}$. Typical uncertainty ~ 0.15 dex

^jStar formation rate, M_{\odot} yr⁻¹. Typical uncertainty ~ 0.2 dex

^kDust reddening $E(B - V)$. Typical uncertainty ~ 0.03

^lAge, 10⁸ yr. Typical uncertainty ~ 0.3 dex

^mTime constant of exponentially declining star-formation history, 10⁸ yr. Typical uncertainty ~ 1 dex

bination rate (e.g., Croft et al. 2002; Kollmeier et al. 2003; Maselli et al. 2004; Desjacques et al. 2004). Figure 15 illustrates this point by comparing the observed distribution of HI absorption among the galaxies in Figure 13 to a preliminary prediction from the windless smooth-particle hydrodynamical (SPH) simulation of Kollmeier et al. (2005, private communication; this simulation is similar to that of Kollmeier et al. 2003 but is matched to the mean redshift of this sample). If the real world resembled the simulations, a 24 galaxy sample would have $n_{\text{obs}} = 7$ or more members with decrement $D < 0.2$ only two times in a thousand (i.e., $\sum_{n_{\text{obs}}=7}^{\infty} \exp(-n_{\text{exp}}) n_{\text{exp}}^{n_{\text{obs}}} / n_{\text{obs}}! \simeq 0.002$, where $n_{\text{exp}} \simeq 1.75$ is the predicted mean number of galaxies with $D < 0.2$ in a 24 object sample).

Although a number of explanations are possible, the data in Figure 15 seem qualitatively consistent with the idea that the galaxies are surrounded by anisotropically expanding winds. Leaking out along the paths of least resistance, these winds would turn moderate absorption

into weak absorption while leaving the strongest absorption systems in place.

Ionizing radiation from any neighboring QSOs might also preferentially eliminate weaker absorption systems. As Figure 16 shows, many of the galaxies with $\bar{f}_{1\text{Mpc}}$ have bright QSOs in their vicinity. Although these QSOs have similar or larger redshifts than the galaxies, as is required for their (presumably) shortlived radiation to have an observable effect on the galaxies’ surroundings (e.g., Figure 12 of Adelberger 2004), the prevalence of neighboring QSOs is not significantly different for galaxies with $\bar{f}_{1\text{Mpc}} \geq 0.5$ and $\bar{f}_{1\text{Mpc}} < 0.5$. Four galaxies of 9 with $\bar{f}_{1\text{Mpc}} \geq 0.5$ have a QSO within $\Delta v = 3000$ km s⁻¹, compared to 2 of 15 with $\bar{f}_{1\text{Mpc}} < 0.5$. The one-sided P -value from Fisher’s (1934) exact test is 0.11, and would increase (i.e., become less significant) if we changed Δv to 2000 km s⁻¹ ($P = 0.25$) or 4000 km s⁻¹ ($P = 0.21$). These numbers could be misleading, however, since even a profound QSO influence might be difficult to detect with significance in a sample so small. More convincing

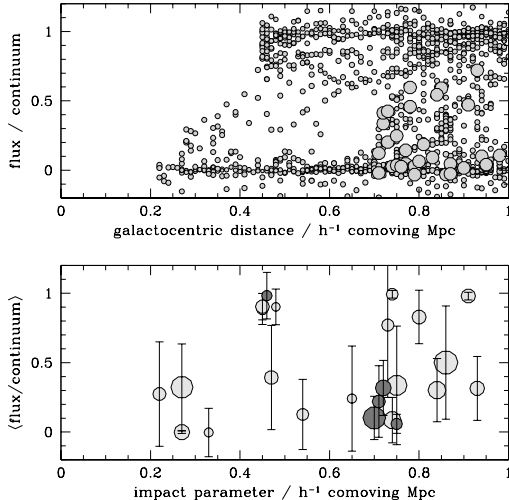


FIG. 13.— Top panel: observed Lyman- α absorption for every QSO-spectrum pixel whose apparent (i.e., redshift space) distance to the nearest galaxy is $r < 1h^{-1}$ comoving Mpc. The circles are larger for lower-resolution spectra; their area is proportional to the wavelength size of the pixel and the smallest pixels have $\Delta\lambda \sim 0.025\text{\AA}$. Bottom panel: the same data grouped by galaxy. The mean transmissivity for the pixels associated with each galaxy is shown on the y axis. Circles are placed on the x axis according to the galaxy’s impact parameter. The area of each circle is proportional to the galaxy’s apparent luminosity in the \mathcal{R} band. Error bars show the rms spread in flux among the pixels with $r < 1h^{-1}$ Mpc. Darker circles are galaxies from Adelberger et al. (2003), re-analyzed after obtaining more-precise galaxy redshifts from near-IR nebular lines. We were able to obtain confirming near-IR nebular redshifts for only one of the galaxies from that paper with $r < 0.5h^{-1}$ comoving Mpc; the other two had redshifts that made near-IR spectroscopy impractical.

is the fact that the QSOs are too faint to alter the ionization balance of material that lies ~ 30 proper Mpc away (i.e., $\Delta v = 2000 \text{ km s}^{-1}$; see, e.g., Adelberger 2004). Their ionizing radiation could explain the galaxies’ weak HI absorption only if the QSOs’ redshifts differ significantly from our estimates.

A search for other explanations would have to explore possible faults with the data themselves. Precise measurements of a galaxy’s redshift are required to recognize that it is associated with a narrow absorption feature in a QSOs spectrum. Any errors in the redshift will tend to move the galaxy away from the feature, artificially reducing the apparent absorption. If such errors were responsible for galaxies with weak absorption, one would expect those galaxies always to have strong absorption features nearby. Figure 16 shows the nearby absorption features for all nine of the galaxies from Figures 13 and 15 that had transmissivity $f_{1\text{Mpc}} > 0.5$. Strong nearby HI absorption is present for about half of the galaxies, but systematic wavelength errors could make our data consistent with the windless simulation only if their magnitude is much worse than the value $\sigma_v = 60 \text{ km s}^{-1}$ that we estimate from repeated observations of individual galaxies.

6. CHARACTERISTICS OF POSSIBLE SUPERWIND GALAXIES

The previous sections discussed two characteristics of intergalactic absorption that might reflect the influence

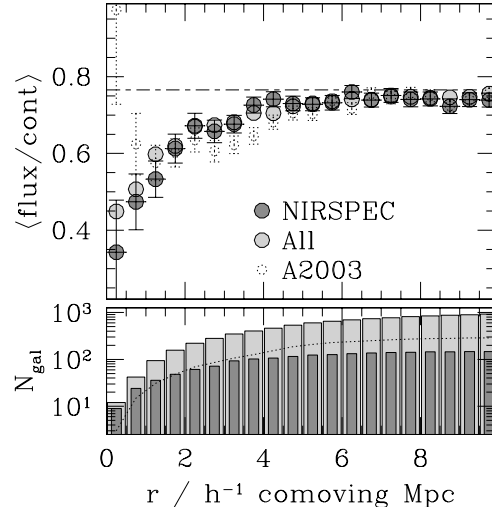


FIG. 14.— Top panel: Mean transmissivity as a function of galactocentric distance. Points at $0 < r < 0.5h^{-1}$ comoving Mpc show the mean transmissivity of all spectral pixels whose redshift-space position lay within $0.5h^{-1}$ comoving Mpc of a galaxy. To scale to a common global transmissivity $\langle f \rangle = 0.765$, the transmissivities of each pixel were multiplied by $\langle f \rangle / c(z)$ before averaging, with $c(z)$ the redshift-dependent smoothed mean transmissivity in each QSO’s spectrum (§ 5). The error bar shows the 1σ uncertainty, estimated by dividing the observed galaxy-to-galaxy scatter in transmissivity by $N_{\text{gal}}^{1/2}$. The points and error bars at larger separations are defined similarly. Darker circles show the result if we restrict ourselves to galaxies with near-IR nebular redshifts. Lighter circles are for the full sample. For comparison, dotted circles show the result of Adelberger et al. (2003) scaled from $\langle f \rangle = 0.67$ to $\langle f \rangle = 0.765$. Bottom panel: the number of galaxies at each separation in each sample.

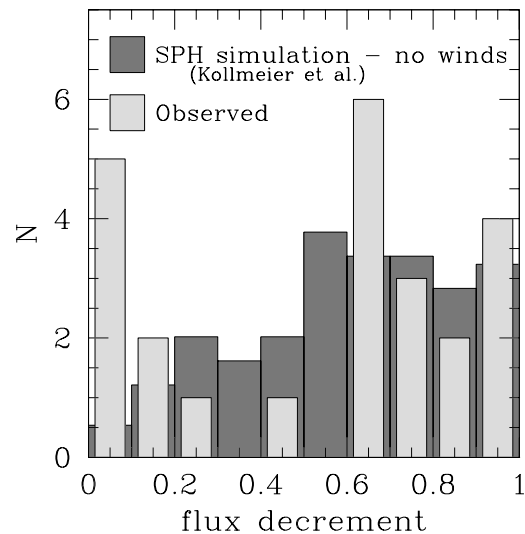


FIG. 15.— Comparison of observed and expected Ly- α absorption near star-forming galaxies. The abscissa shows the flux decrement $1 - f_{1\text{Mpc}}$, where $f_{1\text{Mpc}}$, the mean transmissivity among all pixels within $1h^{-1}$ comoving Mpc of the galaxy, is the quantity shown in the bottom panel of Figure 13. In windless SPH simulations, almost every sightline near a galaxy has strong Lyman- α absorption. This is not observed.

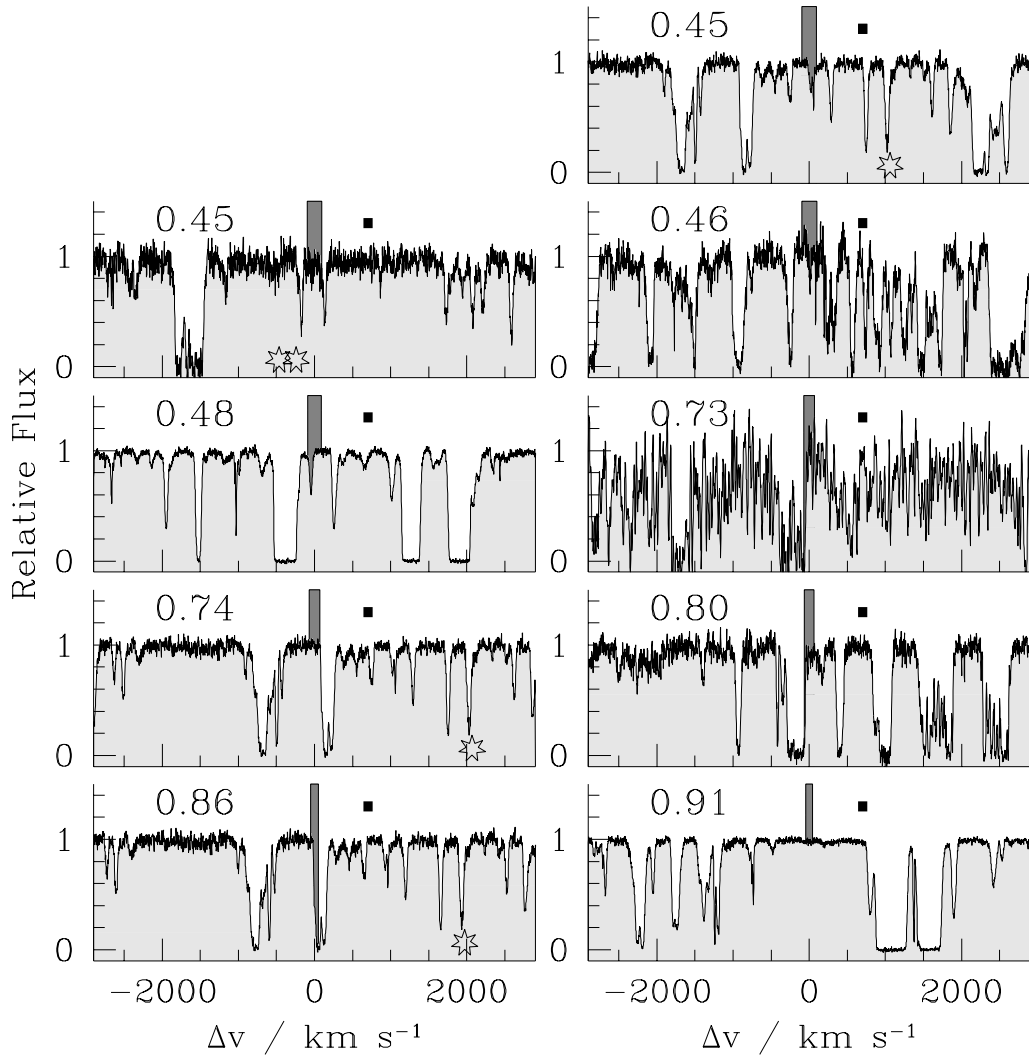


FIG. 16.— HI absorption near the redshifts of the 9 sightline galaxies with the weakest absorption in Figure 13. The lighter shaded region shows the HI absorption in the QSO’s spectrum. The darker shaded box in the background is centered on the galaxy’s redshift. Its width marks the range of pixels that lie within $1h^{-1}$ comoving Mpc of each galaxy. The number to the upper left of each panel gives each galaxy’s impact parameter in h^{-1} comoving Mpc. The redshifts of neighboring QSOs with $G_{AB} < 20.5$ in each field are marked with stars; the QSOs whose spectra are displayed lie at redshifts too high to fall on this plot. The neighboring QSO in the upper right panel and two lowest left panels has $G_{AB} \sim 20.5$ and lies $\sim 9'$ (4 proper Mpc) from the sightline; the two neighboring QSOs in the upper left panel have $G_{AB} = 18.5, 19.5$ and lie $\sim 100'', 600''$ from the sightline. The black square in each panel has a width of 120 km s^{-1} , twice the estimated 1σ uncertainty in each galaxy’s redshift. The largest positive and negative changes in redshift estimate we have encountered when re-observing a galaxy with NIRSPEC, 124 km s^{-1} and -95 km s^{-1} , would displace a galaxy by about this distance.

of a nearby galaxy’s superwind: unusually strong metal absorption or unusually weak HI absorption. The two are contradictory, since metal lines are almost always produced by gas with a large HI column density. The association of either with superwinds could be strengthened if their presence was correlated with properties of the nearby galaxy.

Figure 17 compares various properties of galaxies with $\bar{f}_{1\text{Mpc}} < 0.5$ (lighter bars) and $\bar{f}_{1\text{Mpc}} > 0.5$ (darker bars). Star-formation histories and stellar masses M_* were estimated by fitting model spectral-energy distributions to the galaxies’ observed photometry (U_nGRJK_s + *Spitzer*-IRAC 3.6, 4.5, 5.8, $8.0\mu\text{m}$ for

galaxies in Q1700; U_nGRJK_s for galaxies in Q1623 and Q2343; and U_nGRK_s for the galaxy in Q2346). The models assumed exponentially declining star-formation rates with varying time constants and ages, and each was subjected to a varying amount of reddening by dust that followed a Calzetti (2000) law. See Shapley et al. (2005) and Erb et al. (2005, in preparation) for details. Velocity differences between the galaxies’ interstellar absorption lines, Lyman- α emission line, and nebular emission lines were calculated as in § 2. The rms widths of the nebular lines were estimated by fitting the each line’s profile with a Gaussian and subtracting the resolution in quadrature. Further details can be found in Erb et al. (2004). The

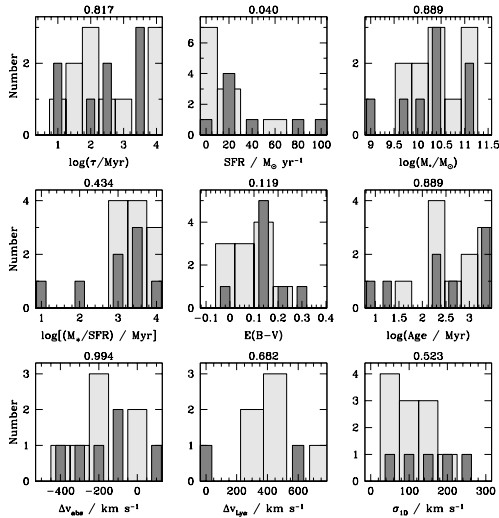


FIG. 17.— Characteristics of galaxies with little nearby intergalactic HI ($f_{\text{HI Mpc}} > 0.5$). The distributions of these galaxies’ properties are shown with dark bars; the distributions for the rest of the $< 1h^{-1}$ Mpc NIRSPEC sample are shown in the light histogram. The number above each panel shows the approximate Kolmogorov-Smirnov probability of observing the data if the two distributions were drawn from the same parent population. This probability is calculated with an approximation (subroutine “probks” in Press et al. 1992) that becomes poor for very small sample sizes (as, e.g., in the bottom center panel.) The abscissae show: τ — time constant in the assumed exponential star-formation history $\text{SFR} \propto e^{-t/\tau}$; SFR — star formation rate; M_* — stellar mass; $E(B-V)$ — dust reddening, for a Calzetti (2000) dust curve; Age — estimated time since beginning of current episode of star-formation; Δv_{abs} — velocity difference between galaxy’s near-IR nebular redshift and its interstellar absorption lines; $\Delta v_{\text{Ly-}\alpha}$ — velocity difference between the near-IR nebular redshift and the Ly- α emission line (which was usually not detected); σ_{1D} — velocity width of the near-IR nebular emission lines.

data in these figures are available in Table 3. Numbers above each panel give the approximate significance of the difference in distributions for the two galaxy populations, calculated with the routine “probks” of Press et al. (1992). Small numbers correspond to more significant differences. None of the differences are especially significant given the number of properties examined, although galaxies with weak nearby HI absorption may have somewhat higher star-formation rates.

Figure 18 is similar, except here the sample is divided by the total detected CIV column density within 200 km s^{-1} of the galaxy redshift. Galaxies with $N_{\text{CIV}} > 10^{13}$ cm^{-2} are indicated with darker bars, the remainder with lighter bars. This differences in this figure may be marginally significant. Galaxies near intergalactic CIV systems appear to have SEDs that require younger ages, shorter time constants, and a wider range of dust reddening. It would be a mistake to interpret this too literally: the parameters have large and correlated uncertainties and our assumed star formation histories are grossly oversimplified. The figure suggests, however, that there are genuine differences between the SEDs of galaxies with and without nearby CIV absorption. The main empirical difference is a bluer mean optical-to-near-IR color for galaxies near CIV systems, which our SED fitting interprets as an excess of A stars relative to F and G stars.

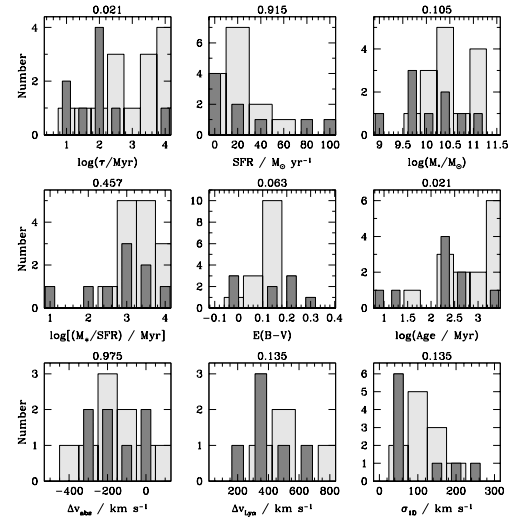


FIG. 18.— Similar to Figure 17, except here we compare galaxies with and without substantial nearby intergalactic CIV absorption. Dark bars are for galaxies with $N_{\text{CIV}} > 10^{13}$ cm^{-2} , where N_{CIV} is the total detected intergalactic CIV column density (cm^{-2}) within 200 km s^{-1} of the galaxy redshift, and light bars are for galaxies with $N_{\text{CIV}} < 10^{13}$ cm^{-2} .

Missing from figures 17 and 18 is any indication of the large-scale environments that contain the different galaxy types. Shot noise prevents us from estimating the local galaxy density near any single object, but we can estimate the mean galaxy density around an ensemble of objects by counting their observed number of galaxy neighbors and dividing by the number expected in the absence of clustering. Figure 19 shows the result for the different galaxy ensembles discussed above. Galaxies in denser environments are more likely to have detectable intergalactic CIV absorption within $1h^{-1}$ comoving Mpc, but local galaxy density does not seem to affect whether a galaxy has $f_{\text{HI Mpc}} > 0.5$ or $f_{\text{HI Mpc}} < 0.5$.

7. DISCUSSION

7.1. Superwinds at $2 \lesssim z \lesssim 3$

Galaxies would presumably be associated with QSO absorption lines even if there were no winds. This subsection discusses how strongly (or weakly) our observations support the existence of superwinds around the galaxies. We consider below the possibility that intergalactic metals were produced at very high redshifts ($z \sim 10$).

The blueshifted absorption and redshifted Lyman- α emission in high-redshift galaxies’ spectra is the strongest evidence for winds from the galaxies. It is expected in a wide range of models in which the stars are surrounded by outflowing gas (e.g., Tenorio-Tagle et al. 1999; Zheng & Miralda-Escudé 2002) and is not (as far as we know) expected in any other class of realistic models. The statistical significance is high, since the same pattern has been observed in the spectra of dozens of galaxies (e.g., figure 1). This observation only shows that the outflowing gas lies somewhere outside the stellar radius, however. It does not imply that the outflow will be driven into the surrounding IGM.

The strength of CIV absorption at $b = 40$ kpc (Figure 5) may suggest that the outflows have normally ad-

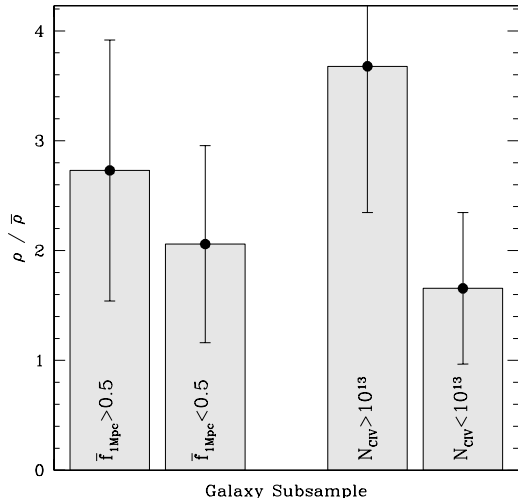


FIG. 19.— Average large-scale environments for different types of galaxies in the $< 1h^{-1}$ Mpc NIRSPEC sample of figure 13. The environment is quantified through the relative local galaxy density $\rho/\bar{\rho}$, which we calculate by counting the number of neighboring galaxies in the full sample within $\Delta\theta = 200''$, $\Delta v = 500 \text{ km s}^{-1}$ of each galaxy in the subsample and dividing by the number expected in the absence of clustering. Galaxies near strong CIV absorbers ($N_{\text{CIV}} > 10^{13} \text{ cm}^{-2}$) tend to reside in denser environments, possibly indicating that the CIV originates outside of the galaxy. In contrast, the prevalence of galaxies with little nearby Ly- α absorption does not appear to be strongly influenced by environment.

vanced to this radius, but even so this is only about half way to the virial radius (for $M_{\text{total}} \sim 10^{12} M_{\odot}$ in the Lambda-CDM cosmology favored by WMAP; Spergel et al. 2003). The minimum allowed velocity range of the gas at $b = 40 \text{ kpc}$ ($\sim 300 \text{ km s}^{-1}$) is not large enough to guarantee escape. In any case the similarity of the CIV absorption strength in Lyman-break Galaxies’ (LBG) spectra and at impact parameter $b = 40 \text{ kpc}$ could just be a coincidence; it does not rule out the idea that the gas at 40 kpc is falling into or orbiting within the galaxy’s potential. Although anisotropies in the galaxy/CIV-system correlation function seem to disfavor infall and favor rapid outflows for the origin of the CIV, CIV systems tend to be found near galaxies which may be too young to have driven winds far into their surroundings. The small number of distinct galaxy-CIV pairs leaves the situation unclear.

Measuring the spatial correlation of galaxies and metals on large (Mpc) scales would seem to provide a powerful way to distinguish between different scenarios for intergalactic metal enrichment. If the metals were produced in LBGs, they should have a spatial bias¹¹ similar to the galaxies’ bias of $b \sim 2.5$ at $z = 3$ (Adelberger et al. 2005). They would have $b = 1$ if they were produced at any redshift by the numerous dwarf galaxies that are 1σ fluctuations, and $b \sim 1.9$ at $z = 3$ if (as envisioned by Madau, Ferrara, & Rees 2001) they were produced at $z = 9$ by galaxies that were 2σ fluctuations. These estimates of the bias exploit Mo & White’s (1996) high-

redshift (i.e., $\Omega \sim 1$) approximation

$$b(z) \simeq 1 + \frac{(\nu^2 - 1)(1 + z)}{1.69(1 + z_i)} \quad (8)$$

for the bias at redshift z of objects that were ν -sigma fluctuations at the earlier redshift z_i . The galaxy-metal cross-correlation length would therefore be equal to the galaxy-galaxy correlation length if the metals were produced by LBGs and smaller for the other two cases. Unfortunately the implied bias for enrichment at $z \sim 10$ depends sensitively on the unknown value of ν . The parameter ν would not have to be very different from the default assumption of Madau, Ferrara, & Rees (2001) to make the bias exactly equal to the bias for enrichment at $z \sim 3$. In any case, we have measured the galaxy-CIV correlation length, not the galaxy-metal correlation length. Our measured cross-correlation function therefore does not have an unambiguous interpretation.

There are only 9 galaxies in our sample with precise (near-IR nebular line) redshifts and little HI within $1h^{-1}$ comoving Mpc, and their statistical significance is even lower than one might imagine. There are two reasons. First, as discussed above, the measurement is difficult. To determine whether a galaxy lies within $\lesssim 1h^{-1}$ Mpc of a narrow absorption line in a QSO spectrum, one needs a good understanding of many possible sources of random and systematic error in the estimated redshifts. In about half the cases there is no absorption line anywhere near the galaxy redshift, but in the remainder the galaxies could conceivably be associated with nearby absorption lines if redshift errors were somewhat larger than we estimate. Reducing the number of galaxies with little nearby HI by 50% would begin to make our observations consistent with the predictions of windless SPH simulations. Second, 5 of the 9 galaxies lie within a single field, Q1623, which contains one of the largest known concentrations of QSOs with $2 \lesssim z \lesssim 3$. This is a consequence of the dense spectroscopic sampling we obtained in the field, but it raises the possibility that our result might have been different had we surveyed a more representative part of the universe. The spatial clustering strength of the high-redshift galaxies in this field is certainly not typical, for example (Adelberger et al. 2005b).

Even without its questionable statistical significance, the apparent lack of HI near some galaxies would not have a straightforward interpretation. This is due to the complexity of the interaction between winds and galaxies’ inhomogeneous surroundings. Analytic models treat this in an extremely crude way, and existing numerical simulations are unable to resolve either the shock fronts or the instabilities that result when the hot wind flows past cooler intergalactic material. As a result it is unclear if winds would destroy the HI near galaxies. Other effects that simulations do not resolve (e.g., cooling instabilities) might reduce the covering fraction of HI near galaxies. Even if there were low-density regions near galaxies in SPH simulations, they might not be recognized since the density is generally estimated by smoothing over the few dozen nearest particles, particles which (by definition) are likely to lie outside of any local under-density. Finally, photoionization could play some role. Kollmeier et al. (2003) and Adelberger et al. (2003) have shown that the galaxies’ radiation cannot destroy all the HI within $1h^{-1}$ comoving Mpc without overpro-

¹¹ on scales larger than the maximum wind radius

ducing the UV background, but photoionizing the weaker clouds around one third of the galaxies might be possible. It therefore remains unclear if the lack of HI near some galaxies is a unique or even an expected signature of superwinds. The weak correlations between galaxy properties and the strength of nearby intergalactic HI absorption may suggest that the HI absorption is unrelated to winds.

7.2. Metal enrichment at $z \sim 10$

Although our observations do not provide unequivocal evidence for superwinds at $2 \lesssim z \lesssim 3$, it would be a mistake to conclude that they favor intergalactic metal enrichment at very high redshifts. In the few cases where the two scenarios have clearly different predictions (e.g., anisotropies in the galaxy-CIV correlation function on small scales), the observations seem to favor lower-redshift enrichment. In addition, enrichment at very high redshifts seems implausible on other grounds. Figure 20 illustrates a major problem: stars that form before $z \sim 10$ probably produce an inconsequential amount of metals compared to the stars that form afterward, so their metals could be dominant in the IGM only if virtually no metals were able to escape into the IGM at later times. In order for 90% of the intergalactic metals observed at $z \sim 3$ to have been produced at $10 \lesssim z \lesssim 15$, for example, supernovae ejecta would have to be at least 100 times more likely to escape their galaxy at $z = 10$ than at $z = 3$. This follows from the fact that the total intergalactic metal density at $z \sim 2$, $\rho_{\text{met}} \simeq \rho_{\text{cr}} \Omega_{\text{met}} \simeq 1.2 \times 10^5 M_{\odot} \text{Mpc}^{-3}$ for $\Omega_{\text{met}} \simeq 4.4 \Omega_C$ and $\Omega_C \simeq 2.3 \times 10^{-7}$ (Schaye et al. 2003), would be roughly twice the total metal production at $10 < z < 15$ and five times smaller than the metal production at $2 \lesssim z \lesssim 5$ if the cosmic star-formation density were roughly constant for $2 < z < 15$, the stellar density at $z \sim 2$ were $\sim 5 \times 10^7 M_{\odot} \text{Mpc}^{-3}$ (e.g., Dickinson et al. 2003; Rudnick et al. 2003), and $100 M_{\odot}$ of star formation produced $1 M_{\odot}$ of metals.

Is the metal escape fraction likely to be 100 times larger at $z \sim 10$ than $z \sim 3$? Two factors are commonly thought to increase the likelihood of escape at high redshift: galaxies are less massive and the intergalactic medium lies closer to them than at later times when the universe has expanded more. Both are offset by competing effects, however, and it is not clear to us that very high redshift galaxies have much of an advantage at all.

First consider the galaxy masses. The gravitational potential energy of a galaxy scales as M^2/r , or $M^{5/3}$, while the energy released by a galaxy's supernovae scales as fM , where f is the efficiency of star formation. If f were independent of M , smaller galaxies would be more easily unbound by supernova explosions. This is the standard assumption, but in fact f increases with M and the situation is not clear cut. For example, compare the star-formation efficiencies of Lyman-break galaxies at $z \sim 3$ to those of galaxies at $z \sim 10$. The ratio of stellar to baryonic mass for Lyman-break galaxies at $z \sim 3$ is $M_*/M_b \sim 0.1$ (Adelberger et al. 2004), which implies $f \sim 0.1$. An upper limit to the star-formation efficiency at $z = 10$ can be derived by assuming that the star-formation density is constant for $2 < z < 15$. (In fact

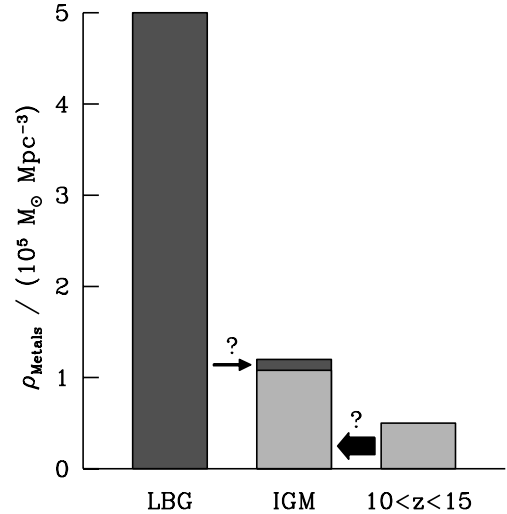


FIG. 20.— The amount of metals produced in massive galaxies at $z \sim 2$ (LBG) compared to the amount of metals in the IGM at $z \sim 2$ and to the estimated maximum amount of metals produced at $10 < z < 15$. Star formation at $10 < z < 15$ probably does not produce enough metals to account for the observed enrichment at $z \sim 2$. Even if it did, the fraction of metals that escape into the IGM would have to be ~ 100 times higher at $10 < z < 15$ than at $z \sim 2-3$ for 90% of the intergalactic metals at $z \sim 2$ to have been produced at $10 < z < 15$.

it appears to be significantly lower at $z \gtrsim 5$; Bunker et al. 2004.) In this case the stellar density at $z = 10$ will be $\Omega_*/\Omega_b = 0.001$, scaling from the $z \sim 2$ stellar density estimated by Dickinson et al. (2003) and Rudnick et al. (2003), while the fraction of baryons in the halos with $v_c \gtrsim 10 \text{ km s}^{-1}$ that are able to host star formation (Dijkstra et al. 2004) is $\Omega_h/\Omega_b \sim 0.08$. That implies an upper limit to the star-formation efficiency of $f \simeq \Omega_*/\Omega_h \sim 0.01$ for typical galaxies at $z \sim 10$. The order-of-magnitude increase in star-formation efficiency at lower redshift removes any advantage higher-redshift galaxies might gain from their smaller masses. A similar argument shows that the star-formation efficiencies of LBGs are far higher than those of smaller galaxies at similar redshifts $2 \lesssim z \lesssim 3$.

Now consider the supposed benefit from the small size of the universe at $z \sim 10$. If supernova ejecta at $z \sim 10$ extended from their galaxies into the receding Hubble flow, their filling fraction at lower redshift would be boosted by the subsequent expansion of the universe. In fact, however, the ejecta will not normally reach the Hubble flow. Instead they are likely to be swept back into their galaxy by the ongoing process of structure formation. To illustrate the point, we show in Figure 21 the distance to the nearest halo of mass $M \gtrsim 10^{11} M_{\odot}$ at $z = 2.12$ for every particle in the GIF-LCDM simulation (Kauffmann et al. 1999) that lay within $1h^{-1}$ comoving Mpc of a galaxy (i.e., halo) at $z = 10$ or $z = 5$. The result is stark: the overwhelming majority of these particles end up inside the virial radius of a galaxy at $z \sim 2$. Since the stalled ejecta of galaxies at $z = 10$ or $z = 5$ will be swept along by the movements of the material that surrounds the galaxies, they should largely end up inside galaxies at $z \sim 2$ as well. This exercise

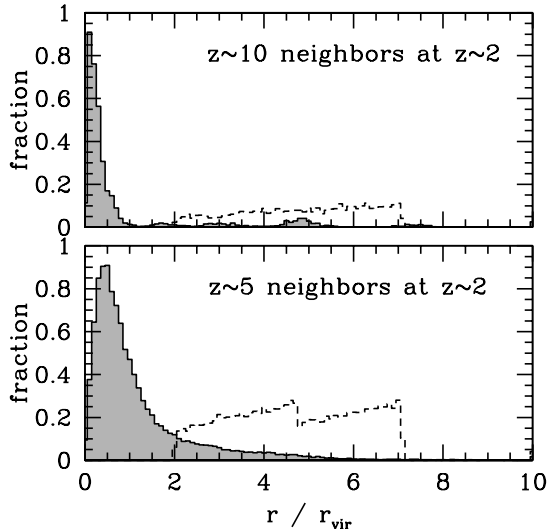


FIG. 21.— Distance to the nearest massive ($M \gtrsim 10^{11} M_{\odot}$) halo at $z \sim 2$ for all GIF-LCDM simulation particles whose distance r to the nearest halo satisfied $2r_{\text{vir}} < r < 1h^{-1}\text{comovingMpc}$ at $z = 10$ (top) or $z = 5$ (bottom). Dashed lines show the particles’ original (higher redshift) distribution of r/r_{vir} ; the solid shaded histograms show the distribution at $z \sim 2$. (The nearest halo and its virial radius are usually significantly different at the initial and final times.) These particles initially lie at larger radii than those expected for the metals ejected by very high redshift winds, yet they mostly end up inside halos by $z \sim 2$. This suggests that the metals ejected at $z \sim 5$ and $z \sim 10$ will generally also lie in massive halos at $z \sim 2$, not in the IGM.

may be slightly misleading, since the GIF-LCDM simulation only resolves halos of mass $M \gtrsim 10^{11} M_{\odot}$ (i.e., $\sim 4\sigma$ fluctuations at $z \sim 10$), not the smaller halos believed to be most responsible for polluting the IGM at $z \sim 10$. However, a simple calculation shows that a significant fraction of the metals from the lower-mass progenitors should also end up inside galaxies at $z \sim 2$. The estimated stalling radius for winds from small galaxies at $z \sim 10$ is ~ 100 comoving kpc (e.g., Madau et al. 2001), which is the Lagrangian radius for a halo of mass $1.7 \times 10^8 M_{\odot}$. If these galaxies’ typical descendants at $z \sim 2$ have masses significantly larger than this, the metals will likely have been swept inside them. According to the extended Press-Schechter formalism, $\sim 85\%$ of the galaxies at $z = 2$ that descended from 2σ fluctuations at $z = 10$ will have masses that exceed this threshold by an order of magnitude (see, e.g., equation 2.16 of Lacey & Cole 1993). A substantial fraction of the metals produced at $10 \lesssim z \lesssim 15$ should therefore be locked inside galaxies by $z \sim 2$. Once there, some of them are likely to cool further, fall towards the center, and disappear from view. Since the total metal production at $10 \lesssim z \lesssim 15$ is at best comparable to the observed metal content of the IGM at $z \sim 2$ (Figure 20), this suggests that the intergalactic metallicity at $z \sim 2$ must receive a significant contribution from some other source. A corollary is that the metal content of the IGM would drain into galaxies and decrease over time if it were not continually replenished. The observed constancy of the IGM metallicity (e.g., Schaye et al. 2003) therefore also seems to require

metals to escape from galaxies at lower redshifts.¹²

8. SUMMARY

We reviewed the status of our search for direct evidence of large-scale outflows around UV-selected star-forming galaxies at $2 \lesssim z \lesssim 3$. These are our principal observations:

- The gas that lies within 40kpc of LBGs produces extremely strong absorption lines ($N_{\text{CIV}} \gg 10^{14} \text{ cm}^{-2}$) in the spectra of background galaxies and QSOs (Figure 5). The large equivalent widths of the CIV absorption in low-resolution spectra imply that the absorbing material has range of velocities of at least $\Delta v = 260 \text{ km s}^{-1}$. The absorption produced by this gas is similar to the interstellar absorption seen in LBGs’ spectra, suggesting the LBGs’ outflowing “interstellar” gas may actually lie at radii approaching 40kpc.

- For roughly half of the LBGs, CIV absorption lines with column density $N_{\text{CIV}} \sim 10^{14} \text{ cm}^{-2}$ are observed out to impact parameters of ~ 80 kpc (Figures 5 and 8). This implies that roughly one-third of all “intergalactic” absorption lines with $N_{\text{CIV}} \gtrsim 10^{14} \text{ cm}^{-2}$ are produced by gas that lies within ~ 80 kpc of an LBG. Galaxies too faint to satisfy our selection criteria could easily account for the remainder. In some cases the absorbing gas has substructure on half-kpc scales (Figure 6).

- The cross-correlation function of galaxies and CIV systems with $N_{\text{CIV}} \gtrsim 10^{12.5} \text{ cm}^{-2}$ appears to be the same as the correlation function of galaxies (Figure 11). This implies that CIV systems and galaxies reside in similar parts of the universe and is consistent with the idea that they are largely the same objects. We also find a strong association of OVI systems with galaxies (Figure 10). On small scales the redshift-space cross-correlation function is highly anisotropic (Figure 12). The metal-enriched gas must therefore have large velocities relative to nearby galaxies. The required velocities appear to exceed the galaxies’ velocity dispersions but are similar to the galaxies’ observed outflow speeds.

- In contradiction to the earlier result of Adelberger et al. (2003), we find that the gas within $1h^{-1}$ comoving Mpc of LBGs usually produces strong Ly- α absorption in the spectra of background galaxies (Figure 14). The absorption is weak (mean transmitted flux within $1h^{-1}$ Mpc of $f_{1\text{Mpc}} > 0.5$) in only about one case out of three (Figure 15). Even so, the weakness of the absorption in these cases remains difficult to understand. Since high-redshift galaxies reside in dense parts of the universe, with large amounts of hydrogen and short recombination times, one would expect them to be surrounded by large amounts of HI. The HI has presumably collapsed into clouds and sightlines to the background QSOs might occasionally miss every cloud near a galaxy, but the SPH

¹² If one removes the assumption that the metals injected into the IGM at a given redshift must lie near galaxies that existed at that redshift, then it is possible to find a spatial distribution of intergalactic metals that matches intergalactic absorption-line statistics and does not drain into galaxies at a significant rate for $2 \lesssim z \lesssim 4$ (e.g., Schaye et al. 2003). The removal of this assumption seems dubious to us, however. Metals could exist in parts of the IGM that were never near galaxies only if they were produced by Population III stars, presumably, and the amount of Population III star formation would have to be inordinately large to match the observed intergalactic metallicity at $z \sim 2$ (e.g., Figure 20; see also Aguirre et al. 2004).

simulations of Kollmeier et al. (in preparation) suggest that the chance of this is very low (Figure 15).

- We were unable to identify any statistically significant differences in age, dust reddening, stellar mass, kinematics, or environment between galaxies with weak nearby HI absorption and the rest, although galaxies with weak absorption may have higher star-formation rates (Figure 17). Galaxies near intergalactic CIV systems appear to reside in relatively dense environments (Figure 19) and to have distinctive SEDs characterized by blue colors and young ages (Figure 18).

As discussed in § 7, none of these observations provide unequivocal evidence for superwinds at $z \sim 2-3$. This is mostly because it is unclear how superwinds would affect the correlation between galaxies and intergalactic absorption lines. Metals and galaxies would lie near each other at $z \sim 3$ even if there were no active outflows, for example. We argued in § 7 that star-formation at $10 < z < 15$ may not produce enough metals to account for the intergalactic metallicity at $z \sim 2-3$, and that many of these metals would be buried inside galaxies by $z \sim 2-3$, but our simple arguments need to be checked with numerical simulations. The interpretation of our data will remain ambiguous until that time. The arguments presented in § 7 should make it clear that metal enrichment at $5 \lesssim z \lesssim 15$ will be much harder to rule out than metal enrichment at $10 \lesssim z \lesssim 15$.

There is only one case where the data seem easy to interpret and we are limited by the small size of our sample. This is the redshift-space distribution of metals within ~ 200 comoving kpc of galaxies. Mapping the velocity offsets between galaxies' stars and their metals

as a function of impact parameter would help show if the detected metals are flowing out of, falling into, or orbiting within the galaxies' halos. The velocity offsets can be mapped by obtaining higher resolution spectra of more close pairs (e.g., the right panel of figure 4) or by obtaining more near-IR nebular redshifts for galaxies near the QSO sightline (e.g., Figure 12). That seems the sensible way to proceed.

Trenchant criticism from P. Madau, P. Petitjean, M. Rauch, J. Schaye, and an anonymous referee improved this paper significantly. We benefited as well from conversations with T. Abel, J. Kollmeier, J. Miralda-Escudé, D. Weinberg and S. White. W. Sargent and M. Rauch gave us generous access to their QSO spectra. J. Kollmeier, D. Weinberg, N. Katz, and R. Davé allowed us to show some of their unpublished results. KLA and AES were supported by fellowships from the Carnegie Institute of Washington and the Miller Foundation. DKE, NAR, and CCS were supported by grant AST 03-07263 from the National Science Foundation and by a grant from the Packard Foundation. During the course of our observations we frequently consulted the NASA/IPAC Extragalactic Database (NED), which is operated by the Jet Propulsion Laboratory, California Institute of Technology, under contract with the National Aeronautics and Space Administration. We are grateful that the people of Hawaii allow astronomers to build and operate telescopes on the summit of Mauna Kea.

REFERENCES

- Adelberger, K.L., Steidel, C.C., Shapley, A.E., & Pettini, M. 2003, *ApJ*, 584, 45
- Adelberger, K.L., Steidel, C.C., Shapley, A.E., Hunt, M.P., Erb, D.K., Reddy, N.A., & Pettini, M. 2004, *ApJ*, 607, 226
- Adelberger, K.L. 2004, *ApJ*, 612, 706
- Adelberger, K.L. 2005, *ApJ*, 621, 574
- Adelberger, K.L., Steidel, C.C., Pettini, M., Shapley, A.E., Reddy, N.A., & Erb, D.K. 2005, *ApJ*, 619, 697
- Adelberger, K.L., Steidel, C.C., Pettini, M., Shapley, A.E., Reddy, N.A., & Erb, D.K. 2005, *ApJ*, 620, L75
- Aguirre, A., Schaye, J., Kim, T.-S., Theuns, T., Rauch, M., & Sargent, W.L.W., 2004, *ApJ*, 602, 38
- Bunker, A.J., Stanway, E.R., Ellis, R.S., & McMahon, R.G. 2004, *MNRAS*, 355, 374
- Calzetti, D., Armus, L., Bohlin, R.C., Kinney, A.C., Koornneef, J., & Storchi-Bergmann, T. 2000, *ApJ*, 533, 682
- Chen, H.-W., Lanzetta, K.M., & Webb, J.K. 2001, *ApJ*, 556, 158
- Croft, R.A.C., Hernquist, L., Springel, V., Westover, M., & White, M. 2002, *ApJ*, 580, 634
- Desjacques, V., Nusser, A., Haehnelt, M.G., & Stoehr, F. 2004, *MNRAS*, 350, 879
- Dickinson, M., Papovich, C., Ferguson, H.C., & Budavári, T., 2003, *ApJ*, 587, 25
- Dijkstra, M., Haiman, Z., Rees, M.J., & Weinberg, D.H., 2004, *ApJ*, 601, 666
- Erb, D.K., Steidel, C.C., Shapley, A.E., Pettini, M., & Adelberger, K.L. 2004, *ApJ*, 612, 122
- Erb, D.K. et al., 2003, *ApJ*, 591, 101
- Fisher, R.A. 1934, "Statistical Methods for Research Workers", 5th Edition, (Edinburgh: Oliver & Boyd), §12
- Franx, M., Illingworth, G.D., Kelson, D.D., van Dokkum, P.G., & Tran, K.-V. 1997, *ApJ*, 486, L75
- Frye, B.L., Broadhurst, T., & Benítez, N. 2002, *ApJ*, 568, 558
- Gnedin, N.Y. 1998, *MNRAS*, 294, 407
- Kaiser, N. 1991, *ApJ*, 383, 104
- Kauffmann, G., Colberg, J.M., Diaferio, A., & White, S.D.M., 1999, *MNRAS*, 303, 188
- Kollmeier, J.A., Weinberg, D.H., Davé, R., & Katz, N. 2003, *ApJ*, 594, 75
- Lacey, C. & Cole, S. 1993, *MNRAS*, 262, 627
- Madau, P., Ferrara, A., & Rees, M.J. 2001, *ApJ*, 555, 92
- Martin, C. 2005, *ApJ*, submitted astro-ph/0410247
- Maselli, A., Ferrara, A., Bruscoli, M., Marri, S., & Schneider, R. 2004, *MNRAS*, 350, 21
- McLean, I.S., Graham, J.R., Becklin, E.E., Figer, D.F., Larkin, J.E., Levenson, N.A., & Teplitz, H.I. 2000, *SPIE*, 4008, 1048
- Mo, H.J. & White, S.D.M. 1996, *MNRAS*, 282, 347
- Oke, J.B. et al. 1995, *PASP*, 107, 3750
- Pettini, M., Kellogg, M., Steidel, C.C., Dickinson, M., Adelberger, K.L., & Giavalisco, M. 1998, *ApJ*, 508, 539
- Pettini, M. et al. 2001, *ApJ*, 554, 981
- Pettini, M., Rix, S.A., Steidel, C.C., Adelberger, K.L., Hunt, M.P., & Shapley, A.E., 2002, *ApJ*, 569, 742
- Ponman, T.J., Cannon, D.B., & Navarro, J.F. 1999, *Nature*, 397, 135
- Press, W. H., Flannery, B. P., Teukolsky, S. A., & Vetterling, W. T. 1992, "Numerical Recipes in C", (Cambridge: Cambridge University Press)
- Quashnock, J.M. & Vanden Berk, D.E. 1998, *ApJ*, 500, 98
- Rauch, M., Sargent, W.L.W., & Barlow, T.A. 2001a, *ApJ*, 554, 823
- Rauch, M., Sargent, W.L.W., Barlow, T.A., & Carswell, R.F. 2001b, *ApJ*, 554, 823
- Rudnick, G. et al., 2003, *ApJ*, 599, 847
- Sargent, W.L.W., Steidel, C.C., & Boksenberg, A. 1988, *ApJS*, 68, 539
- Sheinis, A.I., Miller, J.S., Bolte, M., & Sutin, B.M. 2000, *SPIE*, 4008, 522
- Schaye, J., Aguirre, A., Kim, T., Theuns, T., Rauch, M., & Sargent, W., 2003, *ApJ*, 596, 768
- Shapley, A.E. et al. 2005, *ApJ*, in press
- Shapley, A.E., Steidel, C.C., Pettini, M., & Adelberger, K.L. 2003, *ApJ*, 588, 65
- Simcoe, R.A., Sargent, W.L.W., & Rauch, M. 2002, *ApJ*, 578, 737
- Spergel, D.N. et al. 2003, *ApJS*, 148, 175

- Springel, V. & Hernquist, L. 2003, MNRAS, 339, 289
Springel, V., di Matteo, T. & Hernquist, L. 2004, astro-ph/0409436
Steidel, C.C. 1990, ApJS, 72, 1
Steidel, C.C., Adelberger, K.L., Shapley, A.E., Pettini, M., Dickinson, M., & Giavalisco, M. 2003, ApJ, 592, 728
Steidel, C.C., Shapley, A.E., Pettini, M., Adelberger, K.L., Erb, D.K., Reddy, N.A., & Hunt, M.P. 2004, ApJ, 604, 534
Tenorio-Tagle, G., Silich, S.A., Kunth, D., Terlevich, E., & Terlevich, R. 1999, MNRAS, 309, 332
Vogt, S.S. et al. 1994, SPIE, 2198, 362
Weil, M. L., Eke, V. R., & Efstathiou, G. 1998, MNRAS, 300, 773
White, S.D.M. & Rees, M.J. 1978, MNRAS, 183, 341
Zheng, Z. & Miralda-Escudé, J. 2002, ApJ, 578, 33